Three-dimensional Unstructured Grid Finite-Volume Model for Coastal and Estuarine Circulation and Its Application

Jun Lee[1], Jungwoo Lee[2†], and Sang-Lean Yun[2]

[1]Korea Coastal Ocean Modeling Solutions, South Korea.

[2]Korea Institute of Civil Engineering and Building Technology, South Korea.

†Corresponding author: Jungwoo Lee (jungwoo33@gmail.com)

†Current address: Texas Water Development Board, Austin, Texas, USA

Key Points:

- A new 3D finite volume/difference ocean circulation model is developed.
- Triangular and quadrilateral unstructured grids with the semi-implicit and Eulerian-Lagrangian methods are used to avoid CFL restriction.
- The model was tested with well-known analytical solutions and verified on the Texas coast and comparing to the SCHISM model.

Abstract

We developed a three-dimensional unstructured grid coastal and estuarine circulation model, named the General Ocean Model (GOM). Combining the finite volume and finite difference methods, GOM achieved both the exact conservation and computational efficiency. The propagation term was implemented by a semi-implicit numerical scheme, so-called θ scheme, and the time-explicit Eulerian-Lagrangian Method was used to discretize the non-linear advection term to remove the major limitation of the time step, which appears when solving shallow water equations, by the Courant-Friedrichs-Lewy stability condition. Because the GOM uses orthogonal unstructured computational grids, allowing both triangular and quadrilateral grids, much flexibility to resolve complex coastal boundaries is allowed without any transformation of governing equations. The GOM was successfully verified with five analytical solutions, and it was also validated applying to the Texas coast, showing that overall Skill value of 0.951. The verification results showed that the algorithm used in GOM was correctly coded, and it is efficient and robust.

1. Introduction

This study focuses on the development of a new three-dimensional coastal and estuarine circulation model, and we named this model the General Ocean Model (GOM). GOM was developed by combining finite difference and finite volume numerical schemes, taking advantage of the computational efficiency of the finite difference method (FDM), the exact conservation of finite volume method (FVM), and the flexibility of representing complex geometry with an orthogonal unstructured grid system. The advantage of the unstructured grid system over the structured grid system is obvious, but it requires more simulation effort; i.e., the unstructured mesh system well resolves complex boundaries, on the other hand, the structured grid system is difficult to resolve complex geometries but has a regular structured algebraic equation system and thus it has an efficient solution technique. The refining model grid to better represent a complex coastal geometry enforces modelers to use a small simulation time step to ensure numerical stability. Even though it has been common to use a high-performance computing system, implementing either distributed memory Message Passing Interface (MPI) or shared memory Open Multi-Processing (OpenMP), it is also true that it requires more high simulation costs and longer simulation time by demanding of more dramatic grid refinement. Thus, it is required more efficient numerical schemes and algorithms to adapt the unstructured grid system.

Either significant time constraint with traditional explicit schemes or wave damping with implicit schemes arises when solving shallow water equations. However, the limitation is now well overcome with the semi-implicit approach, so-called θ method, which was successfully adapted in several ocean models (e.g., Unstructured nonlinear Tidal Residual Inter-tidal Mudflat model (UnTRIM) by Casulli and Walters, 2000; Stanford Unstructured Nonhydrostatic Terrain following Adaptive Navier-Stokes Simulator (SUNTANS) by Fringer et al., 2006; Semi-Implicit Cross-Scale Hydroscience Integrated System Model (SCHISM) by Zhang et al., 2015, 2016). Then, another significant bottleneck appears in the nonlinear advection term, and the bottleneck can be successfully removed by using the time-explicit Eulerian-Lagrangian Method (ELM), which is also known as the Semi-Lagrangian (SL) method in the field of the atmospheric modeling. The ELM, which is an unconditionally stable scheme even though it is an explicit method (Starniforth and Cote, 1991), has been getting attention more in the ocean modeling

community since Casulli and Walters (2000) adapted the method in their model, UnTRIM, and successfully applied in San Francisco Bay area (e.g., MacWilliams and Gross, 2013; MacWilliams et al., 2015; MacWilliams et al., 2016).

Distinct features of well-recognized ocean circulation models, which are actively used in the United States of America, are well summarized by Fringer et al. (2019). Each model which introduced by Fringer et al. (2019), has different approaches in horizontal/vertical coordinates systems, numerical schemes, and algorithms when solving governing equations based on the model development purpose. Among those approaches, we greatly benchmarked UnTRIM of Casulli and Walters (2000), and we developed a new three-dimensional (3D) estuarine circulation model including following features to apply our model in general coastal water bodies: (1) unstructured orthogonal triangular and/or quadrilateral horizontal mesh system, (2) z-grid system in vertical, (3) inclusion of winds stress, atmospheric pressure, Coriolis, horizontal/vertical diffusion, and bottom friction, (4) FVM/FDM for equation discretization, (5) ELM for the non-linear advection equation, (6) semi-implicit method for tidal propagation, and (7) wetting and drying. The model we developed here, GOM, is based on well-proven numerical techniques, thus it is robust, accurate, and fast.

2. Governing Equations in GOM

Using the right-handed Cartesian coordinate system (x, y, z) with the vertical origin at the water surface and z-axis points upward, the primitive equation of motion, for the incompressible fluid, with the parameterization of viscous stress terms, with the Boussinesq approximation, and with the hydrostatic assumption, can be written as

Momentum equations:

$$\frac{\partial u}{\partial t} + u\frac{\partial u}{\partial x} + v\frac{\partial u}{\partial y} + w\frac{\partial u}{\partial z} = -g\frac{\partial \eta}{\partial x} - \frac{g}{\rho_o}\int_{z=-h}^{z=\eta}\frac{\partial \rho}{\partial x}dz - \frac{1}{\rho_o}\frac{\partial P_a}{\partial x} + A_h\left(\frac{\partial^2 u}{\partial x^2} + \frac{\partial^2 u}{\partial y^2}\right) + \frac{\partial}{\partial z}\left(A_v\frac{\partial u}{\partial z}\right) + fv \tag{2-1}$$

$$\frac{\partial v}{\partial t} + u\frac{\partial v}{\partial x} + v\frac{\partial v}{\partial y} + w\frac{\partial v}{\partial z} = -g\frac{\partial \eta}{\partial y} - \frac{g}{\rho_o}\int_{z=-h}^{z=\eta}\frac{\partial \rho}{\partial y}dz - \frac{1}{\rho_o}\frac{\partial P_a}{\partial y} + A_h\left(\frac{\partial^2 v}{\partial x^2} + \frac{\partial^2 v}{\partial y^2}\right) + \frac{\partial}{\partial z}\left(A_v\frac{\partial v}{\partial z}\right) - fu \tag{2-2}$$

$$\frac{\partial P}{\partial z} = -\rho g \tag{2-3}$$

Continuity equation:

$$\frac{\partial u}{\partial x}+\frac{\partial v}{\partial y}+\frac{\partial w}{\partial z}=0 \tag{2-4}$$

where $u(x,y,z,t)$, $v(x,y,z,t)$, and $w(x,y,z,t)$ are the velocity components in the horizontal x, y, and vertical z direction, t is time, η is the free surface elevation measured from the vertical origin, P is pressure, P_a is atmospheric pressure, ρ_o is the density of the reference fluid, g is the gravitational acceleration, f is the Coriolis parameter, and A_h and A_v are the horizontal and vertical eddy coefficients, respectively.

Now, we need another form of the continuity equation for the free surface water, and it can be obtained by integrating the original continuity Equation (2-4) over the depth, applying the kinematic surface (i.e., motion at the surface) and bottom boundary conditions (i.e., motion at the bottom). Then, the original continuity Equation (2-4) can be successfully rewritten as a new continuity form for free surface flows (i.e., no rigid boundary at the surface), and this form is called as the "free surface equation"

$$\frac{\partial \eta}{\partial t}+\frac{\partial}{\partial x}\left[\int_{z=-h}^{z=\eta} u dz\right]+\frac{\partial}{\partial y}\left[\int_{z=-h}^{z=\eta} v dz\right]=0 \tag{2-5}$$

3. Unstructured Orthogonal Mesh and Index

We used an unstructured orthogonal mesh, both triangular and quadrilateral mesh, in this model GOM. Once we construct the orthogonal meshes for the study site, the grid system has N_p polygons (cells or elements); note that a definition of an orthogonal unstructured grid is well explained in several previous studies (e.g., Cheng and Casulli, 2001; Fringer et al., 2006). Each grid cell has either three (if it is triangular) or four sides (if it is quadrilateral), and each side has a length of λ. The distance between the centers of neighboring cells, which share the jth side, is denoted by δ_j (Figure 3-1).

As shown in Figure 3-2, along the vertical direction a finite difference discretization, which is not necessarily uniform, is adopted; the kth vertical layer has a height of Δz_k, i.e. the distance between levels $k-1$ and k. The horizontal velocities and water surface elevation are defined at staggered locations as follows. The water surface elevation η_i, the density ρ_i, the salinity S_i, and the temperature T_i are located at the center of the ith polygon; note that the salinity and temperature are not yet included in the current version, but we show this in Figure 3-2 for the clarity and to explain the baroclinic gradient term in the later section. The velocity component normal to each face of a prism is defined at the point of intersection between the face and the segment joining the centers of the two prisms that share the face (i.e. face center).

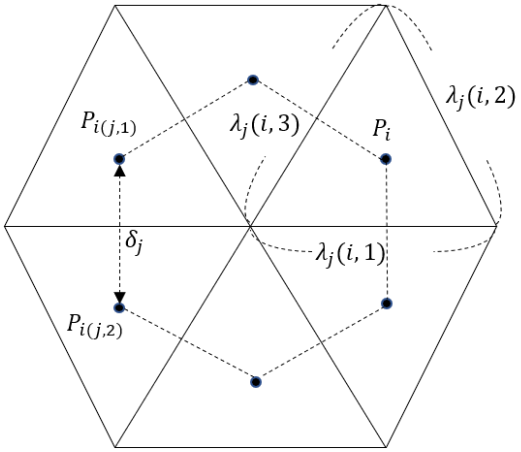

Figure 3-1. Orthogonal unstructured mesh and its notation used in GOM.

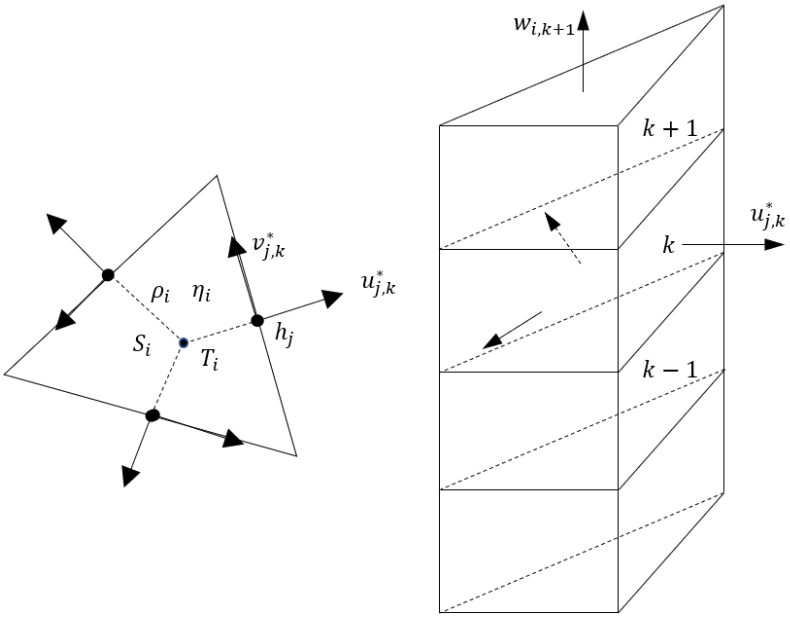

Figure 3-2. Location of computational variables.

4. Finite Volume and Difference Discretization

4.1. Momentum Equations in a New Coordinate

The Equations (2-1) through (2-5) are invariant under solid rotation of the x- and y- axis on the horizontal plane. If we introduce a new coordinate system, x^* and y^*, regarding the cell face, and by using the invariant property of the equations, the horizontal momentum Equations (2-1) and (2-2) can be expressed as follows

$$\frac{\partial u^*}{\partial t} + u^*\frac{\partial u^*}{\partial x} + v^*\frac{\partial u^*}{\partial y} + w\frac{\partial u^*}{\partial z} = -g\frac{\partial \eta}{\partial x} - \frac{g}{\rho_o}\int_{-h}^{\eta}\frac{\partial \rho}{\partial x}dz - \frac{1}{\rho_o}\frac{\partial P_a}{\partial x} + A_h\left(\frac{\partial^2 u^*}{\partial x^2} + \frac{\partial^2 u^*}{\partial y^2}\right) + \frac{\partial}{\partial z}\left(A_v\frac{\partial u^*}{\partial z}\right) + fv^* \quad (4\text{-}1)$$

$$\frac{\partial v^*}{\partial t} + u^*\frac{\partial v^*}{\partial x} + v^*\frac{\partial v^*}{\partial y} + w\frac{\partial v^*}{\partial z} = -g\frac{\partial \eta}{\partial y} - \frac{g}{\rho_o}\int_{-h}^{\eta}\frac{\partial \rho}{\partial y}dz - \frac{1}{\rho_o}\frac{\partial P_a}{\partial y} + A_h\left(\frac{\partial^2 v^*}{\partial x^2} + \frac{\partial^2 v^*}{\partial y^2}\right) + \frac{\partial}{\partial z}\left(A_v\frac{\partial v^*}{\partial z}\right) - fu^* \quad (4\text{-}2)$$

where u^* and v^* are the horizontal velocity components in a new coordinate system, x^* and y^*; note that we omit asterisk $*$ at the x^*- and y^*- coordinates. The relations of velocity components between true horizontal velocities, u and v, and coordinate transformed along each cell face, horizontal velocities, u^* and v^*, are $u = u^*cos\theta - v^*sin\theta$, and $v = u^*sin\theta + v^*cos\theta$, where θ is the angle between the new x- axis, x^*, and the traditional x- axis, x, (Figure 4-1). For simplicity, * is omitted for the equations from now on.

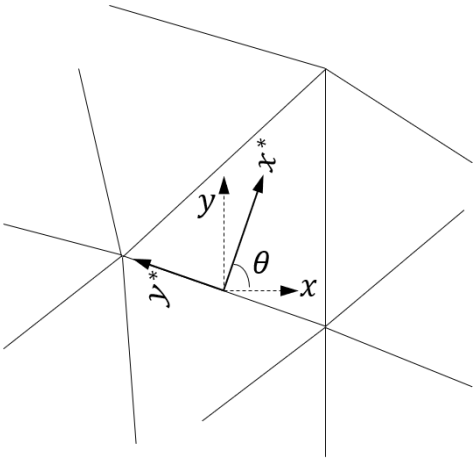

Figure 4-1. Introduction of a new coordinate system.

Each term in Equation (4-1) can be discretized using different methods for the sake of accuracy and efficiency. When solving these equations, the two most significant bottlenecks arise from the barotropic gradient term and the vertical mixing term. Thus, we used the semi-implicit scheme for the barotropic gradient term and the implicit scheme for the vertical diffusion term. On the other hand, the advection, horizontal diffusion, Coriolis, and baroclinic terms are discretized by explicit methods; note that the semi-implicit scheme is also used in the air pressure term. More details in each term are explained in the following sections.

4.1.1. Barotropic Gradient and Vertical Mixing: Implicit Treatment

For the two implicit scheme applied terms, barotropic gradient and the vertical diffusion terms, the finite difference discretization for the velocity component normal to each vertical face of a prism with staggered grid system can be derived from Equation (4-1) and takes the following forms

The barotropic gradient term with a semi-implicit θ scheme:

$$u_{j,k}^{n+1} = u_{j,k}^{n} - g\frac{\Delta t}{\delta_j}\left[\theta\left(\eta_{i(j,2)}^{n+1} - \eta_{i(j,1)}^{n+1}\right) + (1-\theta)\left(\eta_{i(j,2)}^{n} - \eta_{i(j,1)}^{n}\right)\right] \tag{4-3}$$

The vertical diffusion term with the implicit scheme:

$$u_{j,k}^{n+1} = u_{j,k}^{n} + \frac{\Delta t}{\Delta z_{j,k}^{n}}\left[A_{v\,j,k+1/2}\frac{u_{j,k+1}^{n+1} - u_{j,k}^{n+1}}{\Delta z_{j,k+1/2}^{n}} - A_{v\,j,k-1/2}\frac{u_{j,k}^{n+1} - u_{j,k-1}^{n+1}}{\Delta z_{j,k-1/2}^{n}}\right] \tag{4-4}$$

Then, Equation (4-1) can be written as

$$\begin{aligned} u_{j,k}^{n+1} = u_{j,k}^{n} + F_{j,k}^{n} \\ -g\frac{\Delta t}{\delta_j}\left[\theta\left(\eta_{i(j,2)}^{n+1} - \eta_{i(j,1)}^{n+1}\right) + (1-\theta)\left(\eta_{i(j,2)}^{n} - \eta_{i(j,1)}^{n}\right)\right] \\ + \frac{\Delta t}{\Delta z_{j,k}^{n}}\left[A_{v\,j,k+1/2}\frac{u_{j,k+1}^{n+1} - u_{j,k}^{n+1}}{\Delta z_{j,k+1/2}^{n}} - A_{v\,j,k-1/2}\frac{u_{j,k}^{n+1} - u_{j,k-1}^{n+1}}{\Delta z_{j,k-1/2}^{n}}\right] \end{aligned} \tag{4-5}$$

where $k = m_j, m_j + 1, \ldots, M_j^n$, thus m_j and M_j^n denote the lower and upper limit for the vertical k index at j-th side and time step n. The $u_{j,k}^n$ is the horizontal velocity component normal to the j-th side of the i-th mesh (we omit the subscript i in equations for convenience), at vertical level k and time step n; F is an explicit finite difference operator, which includes the remained terms in Equation (4-1): nonlinear advection, baroclinic gradient, air pressure, horizontal diffusion, and Coriolis terms. In this model, the nonlinear advection term and the Coriolis term are calculated by ELM, and the horizontal diffusion term is calculated by the finite volume cell-centered method, the air pressure term is calculated by the semi-implicit, θ, method, and the baroclinic gradient term is calculated by the explicit method; calculations of the term $F_{j,k}^n$ will be discussed in following sections.

4.1.2. Nonlinear Advection: ELM

The Eulerian-Lagrangian Method is used for solving the nonlinear advection terms in the Equations (4-1) and (4-2) to take advantage of its simplicity and the enhanced stability and accuracy. The ELM is well introduced by other researchers (e.g., Cheng et al., 1984; Oliveira and Baptista, 1998; Lentine et al., 2010), however, we introduced the approach again for the clarity. Most of the fundamental equations in fluid dynamics can be derived from principles in either Eulerian form or Lagrangian form. Eulerian equations describe the evolution that would be observed at a fixed point in space while Lagrangian equations describe the evolution of the flow that would be observed following the motion of an individual parcel of fluid. Consider the diffusion-free non-conservative advection equation in 1D

$$\frac{\partial c}{\partial t} + u\nabla c = 0 \tag{4-6}$$

where the $c(x,t)$ represents any scalar quantities or velocity vectors, u is the velocity field, and ∇ is a gradient operator. Then, the one-dimensional Eulerian advection Equation (4-6) can be expressed in the Lagrangian form as

$$\frac{Dc}{Dt} = 0 \tag{4-7}$$

The mathematical equivalence of Equations (4-6) and (4-7) follows from the definition of the total derivative,

$$\frac{D}{Dt} = \frac{\partial}{\partial t} + \frac{dx}{dt}\frac{\partial}{\partial x} \tag{4-8}$$

and the definition of the velocity,

$$\frac{dx_i}{dt} = u_i^*(x_1, x_2, x_3) \tag{4-9}$$

where $i = 1$, 2, and 3 and * represents a linear interpolant between time step n and $n+1$. When a Lagrangian numerical treatment is applied to Equation (4-7), the computational grid will be continuously deforming in the general case when u is non-constant. For operational advantage, however, we will discretize Equation (4-7) on a fixed Eulerian grid system. Let's consider one-dimensional time-dependent grid in Eulerian grid shown in Figure 4-2. A finite difference scheme for Equation (4-6) is simply

$$c_i^{n+1} = c_{i-a}^n \tag{4-10}$$

where $c_{i-a}^n = c[(i-a)\Delta x, n\Delta t]$ and n is time step, i is any mesh or grid point, t is the index at a grid point, and a is the CFL number. In general, the CFL number is not an integer, therefore $(i-a)$ is not the index of a grid point and a proper interpolation formula should be used to define c_{i-a}^n. The stability, numerical diffusion, and unphysical oscillations of Equation (4-10) depend on the interpolation formula chosen. If a linear interpolation between $(i\text{-}\,n\text{-}\,1)$ and $(i\text{-}\,n)$ is used to estimate c_{i-a}^n, one obtaines the first order upwind scheme. If a quadratic polynomial fit is used to interpolate between $(i\text{-}\,n\text{-}\,1)$, $(i\text{-}\,n)$, and $(i\text{-}\,n\text{+}\,1)$, one obtains the Leith's (1971) method.

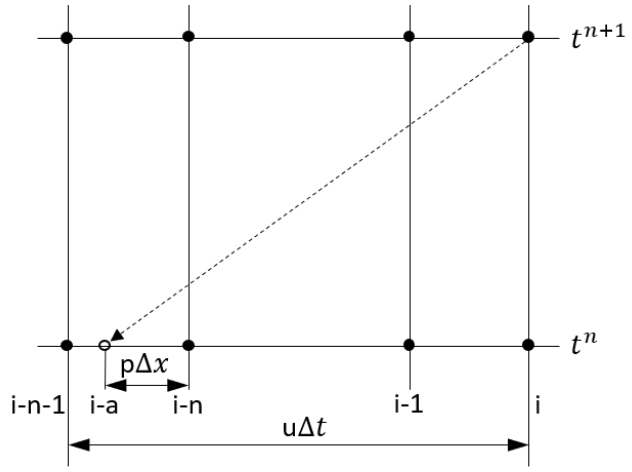

Figure 4-2. Schematic diagram for Eulerian grid on the Lagrangian frame.

The ELM uses a generalization of the interpolation concept of c_{i-a}^n between two or more grid points which do not necessarily include the point (i). Consider that c_{i-a}^n is taken to be a linear interpolation using one node upstream and one downstream. For a given $a \geq 0$ let n be the integer part of a and p the decimal part, then $a = n + p,\ 0 \leq p < 1$. In this case, Equation (4-10) becomes

$$c_i^{k+1} = c_{i-n}^k - p\left(c_{i-n}^k - c_{i-n-1}^k\right) = c_{i-a}^k \tag{4-11}$$

Note that if $a < 1$, then n=0, p= a, and finite difference equations of Equation (4-11) reduces to the first-order upwind method since $0 \leq p < 1$.

Since the velocity u is generally non-uniform, the correct value of a can be found from the solution of the ordinary differential Equation (4-9) in three-dimension using any backward trajectory computation. The velocity u is known only at time level t^n to t^{n+1}. The tracking method and associated error analysis are well-reviewed by Oliveira and Baptista (1998). In this study, the backward Euler methods (both one-step backward Euler and multi-step backward Euler methods) are used for computation of the trajectory. To trace the Lagrangian trajectory, a three-dimensional solution of Equation (4-9) is required, and backtracking for the velocity starts from the element's face. To compute the Lagrangian velocity, the time step Δt is divided into N equal increments, $\tau = \Delta t/N$, and Equation (4-9) is discretized backward as

$$x^{s-1} = x^s - \tau u^k(x^s), \ \text{where}\ x^N = x_i, \qquad s = N, N-1, N-2, \ldots, 2, 1 \tag{4-12}$$

where $u^k(x^s)$ is interpolated with any interpolation formula. Then, at x_i, a can be defined by

$$a = \frac{x_i - x^0}{\Delta t} \tag{4-13}$$

Figure 4-3 illustrates the backtracking of the Lagrangian trajectory for an unstructured mesh. The superscript * here denotes a variable evaluated at the time t^n at the end of the Lagrangian trajectory from a computational node. Tracking begins at an element face of velocity node and

Equation (4-9) is used to find the foot of the Lagrangian trajectory. Once the foot of the Lagrangian trajectory is found, the Eulerian velocity is evaluated by the following interpolation function.

$$\begin{aligned} U_{j(i,l),k}^{t+\Delta t} &= U_{j(i-a,l),k-b}^{t} \\ &= (1-p)\left[(1-q)U_{j(i,l),k}^{*t} + qU_{j(i,l),k-1}^{*t}\right] \\ &\quad + p\left[(1-q)U_{j(i-1,l),k}^{*t} + qU_{j(i-1,l),k-1}^{*t}\right] \end{aligned} \tag{4-14}$$

where

$$p = -U_{j(i,l),k}^{t}\frac{\Delta t}{\delta_j} \tag{4-15}$$

and

$$q = -w_{j(i,l),k}^{t}\frac{\Delta t}{\Delta z} \tag{4-16}$$

Equations (4-15) and (4-16) are solved in the same manner as a method to solve Equation (4-12). Finally, the non-linear term (NL) in the governing equation is approximated by Equation (4-14) as

$$NL = U_{j(i-a,l),k-b}^{t} \tag{4-17}$$

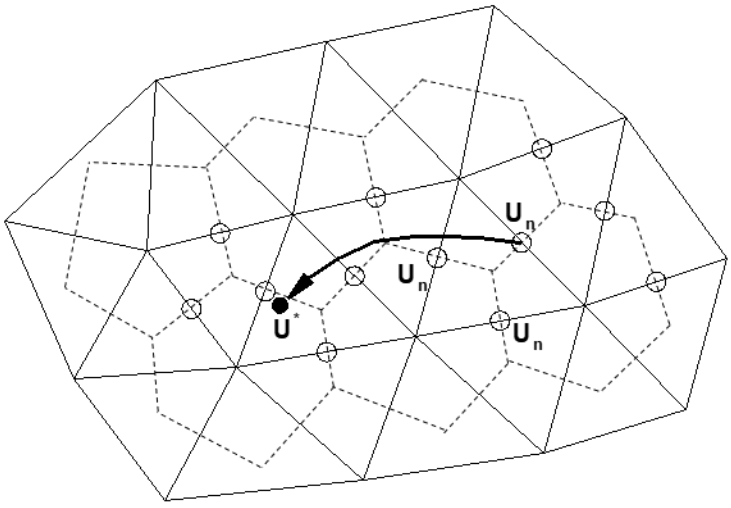

Figure 4-3. Schematic diagram of backtracking for the Lagrangian trajectory.

229 4.1.3. Coriolis: ELM

230 The Coriolis term in the equation is treated with the explicit ELM to take advantage of no
231 time limitation for numerical stability. Consider the Coriolis term in Equation (4-1)

$$\frac{\partial u}{\partial t} = fv \tag{4-18}$$

232 By the explicit ELM, Equation (4-18) can be discretized as

$$u_{j,k}^{n+1} = u_{j,k}^{n} + \Delta t f v_{j,k}^{*} \tag{4-19}$$

233 where v^* is the tangential velocity component in a right-hand coordinate system obtained by the
234 Eulerian-Lagrangian Method (see Figure 4-1). Finally, the Coriolis term (COR) in the Equation
235 (4-1) is discretized by

$$COR = \Delta t f v_{j,k}^{*} \tag{4-20}$$

236 4.1.4. Horizontal Diffusion: Finite Volume Cell-Centered Method

237 The conservation laws of fluid motion may be expressed mathematically in either
238 differential or integral forms. When the integral form of the equation is utilized, the
239 discretization of the equations is the finite volume method. To generalize the method, consider a
240 two-dimensional heat conduction equation

$$\frac{\partial T}{\partial t} = A_h \left(\frac{\partial^2 T}{\partial x^2} + \frac{\partial^2 T}{\partial y^2} \right) \tag{4-21}$$

241 Then, the Equation (4-21) can be written as a conservative form

$$\frac{\partial T}{\partial t} = A_h \left[\frac{\partial}{\partial x} \left(\frac{\partial T}{\partial x} \right) + \frac{\partial}{\partial y} \left(\frac{\partial T}{\partial y} \right) \right] \tag{4-22}$$

242 Define $F = \left(\frac{\partial T}{\partial x} \right)$ and $G = \left(\frac{\partial T}{\partial y} \right)$, then Equation (4-22) is written as

$$\frac{\partial T}{\partial t} = A_h \left[\frac{\partial F}{\partial x} + \frac{\partial G}{\partial y} \right] \tag{4-23}$$

243 Equation (4-23) is integrated over an element's area such as quadrilateral mesh or
244 triangular mesh, then we have

$$\int_{P_i} \left(\frac{\partial T}{\partial t} \right) dxdy = A_h \int_{P_i} \left(\frac{\partial F}{\partial x} + \frac{\partial G}{\partial y} \right) dxdy \tag{4-24}$$

245 where P_i denotes the i-th polygon. Subsequently, Green's Theorem is applied to the right-hand
246 side of Equation (4-24). Recall that Green's Theorem converts area integrals to line integrals.
247 Thus, Equation (4-24) is written as

$$\int_{P_i}\left(\frac{\partial T}{\partial t}\right)dxdy = A_h \oint_{P_i}(Fdy - Gdx) \tag{4-25}$$

Finally, Equation (4-25) can be approximated as

$$T_i^{n+1} = T_i^n + A_h \frac{\Delta t}{A_i}\oint_{P_i}(Fdy - Gdx) \tag{4-26}$$

Thus, the horizontal diffusion term (HD) in the Equation (4-1) is approximated as:

$$HD = A_h \frac{\Delta t}{P_i}\left(\oint_{P_i}(Fdy - Gdx)\right) \tag{4-27}$$

4.1.5. Atmospheric Pressure: Semi-implicit Method

The atmospheric pressure term in the Equation (4-1) is approximated by the semi-implicit, θ, method in time and forward difference in space. Consider the atmospheric pressure term in Equation (4-1)

$$\frac{\partial u}{\partial t} = -\frac{1}{\rho_o}\frac{\partial P_a}{\partial x} \tag{4-28}$$

The semi-implicit in time and forward differencing in spatial derivative produces the following finite difference equation of the form

$$\frac{u_{j,k}^{n+1} - u_{j,k}^n}{\Delta t} = -\frac{1}{\rho_o}\left(\frac{P_{a\,i(j,2)}^{n+\theta} - P_{a\,i(j,1)}^{n+\theta}}{\delta_j}\right) \tag{4-29}$$

and the atmospheric pressure term (AP) in the Equation (4-1) is approximated as

$$AP = -\frac{\Delta t}{\rho_o}\left(\frac{P_{a\,i(j,2)}^{n+\theta} - P_{a\,i(j,1)}^{n+\theta}}{\delta_j}\right) \tag{4-30}$$

The stability analysis indicates that this method is stable when $0.5 \le \theta \le 1$. The values of $P_a^{n+\theta}$ are not calculated but provided explicitly as data each time step.

4.1.6. Baroclinic Gradient: Explicit

The baroclinic gradient term (*BG*) in Equation (4-1) can be discretized with the explicit scheme

$$u_{j,k}^{n+1} = u_{j,k}^n - g\frac{\Delta t}{\rho_o \delta_j}\left[\sum_{k=kk}^{M}\Delta z_{j,k}^n\left(\rho_{i(j,2),k}^n - \rho_{i(j,1),k}^n\right) - \frac{\Delta z_{j,kk}^n}{2}\left(\rho_{i(j,2),kk}^n - \rho_{i(j,1),kk}^n\right)\right] \tag{4-31}$$

Then, the final numerical discretization of explicit term F in Equation (4-5), is written as

$$F_{j,k}^{n} = NL + HD + COR + AP + BG \tag{4-32}$$

4.2. Boundary Treatment

4.2.1. Surface and Bottom Boundary Treatment for the Vertical Diffusion Term

While the vertical diffusion term in Equation (4-5) applies for a middle of a water column, new relations require at both surface and bottom boundary layers, to accelerate by the wind stress and to retard by the bottom friction. Using the shear stress, the vertical boundary conditions at the surface and the bottom yield following formulae

$$A_{v\,j,M+1/2}\frac{u_{j,M+1}^{n+1}-u_{j,M}^{n+1}}{\Delta z_{j,M+1/2}^{n}} = \gamma_T^{n+1}\left(u_{j,air}^{n+1} - u_{j,M}^{n+1}\right), \text{ at the surface} \tag{4-33}$$

$$A_{v\,j,m-1/2}\frac{u_{j,m}^{n+1}-u_{j,m-1}^{n+1}}{\Delta z_{j,m-1/2}^{n}} = \gamma_B^{n+1}\left(u_{j,m}^{n+1} - 0\right), \text{ at the bottom} \tag{4-34}$$

where m and M denote the bottom and top layers, respectively, and $\gamma_T^{n+1} = \frac{Av_{j,M+1/2}^{n}}{\Delta z_{j,M+1/2}^{n}}$, and $\gamma_B^{n+1} = \frac{Av_{j,m-1/2}^{n}}{\Delta z_{j,m-1/2}^{n}}$.

At the bottom, we used the Chezy-Manning formula

$$\rho_o A_v \frac{\partial u}{\partial z} = \tau_{bx} = \rho_o \gamma_B u_m \tag{4-35}$$

$$\rho_o A_v \frac{\partial v}{\partial z} = \tau_{by} = \rho_o \gamma_B v_m \tag{4-36}$$

where $\gamma_B = C_{db}\sqrt{(u^2+v^2)} = \frac{g}{Cz^2}\sqrt{(u^2+v^2)}$, u and v are velocities at the bottom layer, and Cz is the Chezy friction coefficient which can be formulated as

$$\mathrm{Cz} = \frac{R^{1/6}}{n} \approx \frac{H^{1/6}}{n} \tag{4-37}$$

where R is the hydraulic radius and n is the Manning's roughness coefficient, and in shallow estuaries, the hydraulic radius can be approximated by the total depth H. Then, $\gamma_B = C_{db}\sqrt{u_m^2 + v_m^2}$, and it is a non-negative bottom stress coefficient that depends on the velocity at the bottom layer (Casulli and Walters, 2000).

Similarly, the boundary conditions at the free surface are specified by the prescribed wind stresses

$$\rho_o A_v \frac{\partial u}{\partial z} = \tau_{wx} = \rho_{air} C_{da} u_w \sqrt{u_w^2 + v_w^2} = \rho_{air} \gamma_T u_w \tag{4-38}$$

$$\rho_o A_v \frac{\partial v}{\partial z} = \tau_{wy} = \rho_{air} C_{da} v_w \sqrt{u_w^2 + v_w^2} = \rho_{air} \gamma_T v_w \tag{4-39}$$

where τ_{wx} and τ_{wy} are the wind stresses in x and y directions at the free surface; u_w and v_w are the components of wind speed measured at some distance above the free surface, and C_{da} is the surface drag coefficient. The surface drag coefficient is calculated by the empirical relationship developed by either Garratt (1977) or Smith (1980) in our model

$$C_{da} = 0.001(0.75 + 0.067W_s), \text{ Garratt (1977)} \tag{4-40}$$

$$C_{da} = 0.001(0.61 + 0.063W_s), \text{ Smith (1980)} \tag{4-41}$$

where W_s is the wind speed measured at 10 meters above the water surface. Then, $\gamma_T = C_{da} \frac{\rho_{air}}{\rho_o} \sqrt{u_w^2 + v_w^2}$, which is a non-negative wind stress coefficient that depends on the wind speed (Casulli & Walters, 2000).

4.2.2. Treatment of Open Boundary Conditions

The tidal open boundary condition for the surface elevation is prescribed by

$$\eta(x, y, t) = \sum_{n=1}^{N} a_n cos\left(\frac{2\pi}{T_n} t + \phi_n\right) \tag{4-42}$$

where a_n, T_n, and ϕ_n are the amplitude, period, and phase angle of each tidal constituent. When open boundary conditions are provided in terms of the surface elevation, the normal velocity component is assumed to be of a zero slope while the tangential velocity component may be either (1) zero, (2) zero slope, or (3) computed from the momentum equations. In this model, it is assumed that the velocity gradients are zero at the open boundary.

4.3. Free Surface Equation

To obtain complete local and global mass conservation and stability, the free surface Equation (2-5) is discretized by the finite volume method. Consider a uniform rectangular mesh as shown in Figure 4-4. To get a semi-implicit finite volume equation, integrate Equation (2-5) over an area of an element P_i, then

$$\int_{P_i} \left(\frac{\partial \eta}{\partial t}\right) \Delta x \Delta y = -\int_{P_i} \left(\frac{\partial}{\partial x}\left[\int_{-h}^{\eta} u dz\right] + \frac{\partial}{\partial y}\left[\int_{-h}^{\eta} v dz\right]\right) \Delta x \Delta y \tag{4-43}$$

Now, a semi-implicit finite volume discretization for Equation (4-43) gives

$$\begin{aligned}\left(\frac{\eta_i^{n+1}-\eta_i^n}{\Delta t}\right)\Delta x\Delta y &= -\theta\left[\left(\frac{\sum_{k=m}^{M}\Delta z_{j(i,1),k}^{n}u_{j(i,1),k}^{n+1}-\sum_{k=m}^{M}\Delta z_{j(i,3),k}^{n}u_{j(i,3),k}^{n+1}}{\Delta x}\right)\Delta x\Delta y\right.\\ &\left.+\left(\frac{\sum_{k=m}^{M}\Delta z_{j(i,2),k}^{n}u_{j(i,2),k}^{n+1}-\sum_{k=m}^{M}\Delta z_{j(i,4),k}^{n}u_{j(i,4),k}^{n+1}}{\Delta \mathrm{y}}\right)\Delta x\Delta y\right]\\ &-(1-\theta)\left[\left(\frac{\sum_{k=m}^{M}\Delta z_{j(i,1),k}^{n}u_{j(i,1),k}^{n}-\sum_{k=m}^{M}\Delta z_{j(i,3),k}^{n}u_{j(i,3),k}^{n}}{\Delta x}\right)\Delta x\Delta y\right.\\ &\left.+\left(\frac{\sum_{k=m}^{M}\Delta z_{j(i,2),k}^{n}u_{j(i,2),k}^{n}-\sum_{k=m}^{M}\Delta z_{j(i,4),k}^{n}u_{j(i,4),k}^{n}}{\Delta \mathrm{y}}\right)\Delta x\Delta y\right]\end{aligned} \tag{4-44}$$

where $\Delta x = \lambda_{j(i,2)} = \lambda_{j(i,4)}$ and $\Delta \mathrm{y} = \lambda_{j(i,1)} = \lambda_{j(i,3)}$.

If Equation (4-44) is generalized for any shape of polygons, a semi-implicit finite volume discretization for the free surface equation at the center of each polygon is taken to be following form (Casulli and Walters, 2000)

$$\begin{aligned}P_i\eta_i^{n+1} &= P_i\eta_i^n-\theta\Delta t\sum_{l=1}^{S_i}\left[S_{i,l}\lambda_{j(i,l)}\sum_{k=m}^{M}\Delta z_{j(i,l),k}^{n}\,u_{j(i,l),k}^{n+1}\right]\\ &-(1-\theta)\Delta t\sum_{l=1}^{S_i}\left[S_{i,l}\lambda_{j(i,l)}\sum_{k=m}^{M}\Delta z_{j(i,l),k}^{n}\,u_{j(i,l),k}^{n}\right]\end{aligned} \tag{4-45}$$

where P_i denotes the area of the i-th polygon, i.e. $P_i = \Delta x \times \Delta y$ in Figure 4-4, and $S_{i,l}$ is a sign function of flows at each side, which defined as (Casulli and Walters, 2000)

$$S_{i,l} = \frac{i[j(i,l),2]-2i+i[j(i,l),1]}{i\big[j(i,l),2\big]-i[j(i,l),1]\big]} \tag{4-46}$$

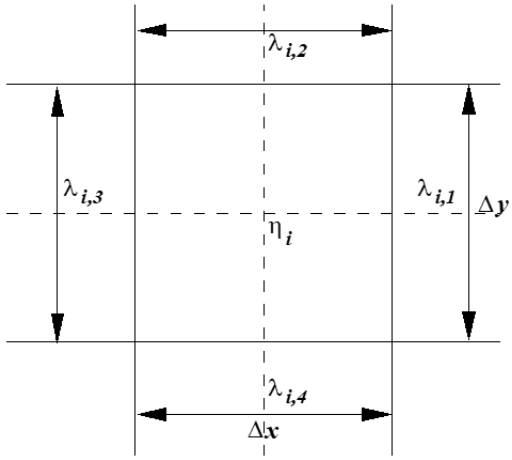

Figure 4-4. Numerical stencils of a rectangular grid for the Finite Volume Method.

5. Solution Algorithm

5.1. Solution of Governing Equations

Including wind stress at the surface layer and bottom stress at the bottom layer, and re-arranging the original x-momentum Equation (4-5), then we have the following tridiagonal matrix form for the i-th water column from the surface to the bottom layer at the j-th side

$$A_j^n U_j^{n+1} = G_j^n - \theta g \frac{\Delta t}{\delta_j}\left[\eta_{i(j,2)}^{n+1} - \eta_{i(j,1)}^{n+1}\right]\Delta Z_j^n \tag{5-1}$$

where

$$A_j^n = \begin{bmatrix} (\Delta t\gamma_T^{n+1} + \Delta z_{j,M}^n + a_{j,M-1/2}^n) & -a_{j,M-\frac{1}{2}}^n & & & \\ -a_{j,M-\frac{1}{2}}^n & (a_{j,M-\frac{1}{2}}^n + \Delta z_{j,M-1}^n + a_{j,M-\frac{3}{2}}^n) & -a_{j,M-3/2}^n & & \\ & \ddots & \ddots & \ddots & \\ & & -a_{j,m+1/2}^n & (a_{j,m+\frac{1}{2}}^n + \Delta z_{j,m}^n + \Delta t\gamma_B^{n+1}) \end{bmatrix}, \tag{5-2}$$

$$U_j^{n+1} = \begin{bmatrix} u_{j,M}^{n+1} \\ u_{j,M-1}^{n+1} \\ \vdots \\ u_{j,m}^{n+1} \end{bmatrix}, \qquad \Delta Z_j^n = \begin{bmatrix} \Delta z_{j,M}^n \\ \Delta z_{j,M-1}^n \\ \vdots \\ \Delta z_{j,m}^n \end{bmatrix},$$

$$G_j^n = \begin{bmatrix} \Delta z_{j,M}^n \left\{ F_{j,M}^n - g\frac{\Delta t}{\delta_j}(1-\theta)\left(\eta_{i(j,2)}^n - \eta_{i(j,1)}^n\right)\right\} + \Delta t \gamma_T^{n+1} u_{j,air}^{n+1} \\ \Delta z_{j,M-1}^n \left\{ F_{j,M-1}^n - g\frac{\Delta t}{\delta_j}(1-\theta)\left(\eta_{i(j,2)}^n - \eta_{i(j,1)}^n\right)\right\} \\ \vdots \\ \Delta z_{j,m}^n \left\{ F_{j,m}^n - g\frac{\Delta t}{\delta_j}(1-\theta)\left(\eta_{i(j,2)}^n - \eta_{i(j,1)}^n\right)\right\} \end{bmatrix},$$

with $a_{j,k\pm1/2}^n = \Delta t \frac{A_{v\,j,k\pm1/2}^n}{\Delta z_{j,k\pm1/2}^n}$, $\gamma_B = C_{db}\sqrt{u_m^2 + v_m^2}$, and $\gamma_T = C_{da}\sqrt{u_w^2 + v_w^2}$.

If we substitute U_j^{n+1} from Equation (5-1) into Equation (4-45), which is the free surface wave equation, and rearrange the equation, then we have

$$\begin{aligned} &P_i\eta_i^{n+1} - g\Delta t^2\theta^2 \sum_{l=1}^{S_i} \frac{\lambda_{j(i,l)}}{\delta_{j(i,l)}} [(\Delta Z)^T A^{-1} \Delta Z]_{j(i,l)}^n \left(\eta_{i[j(i,l),2]}^{n+1} - \eta_{i[j(i,l),1]}^{n+1}\right) \\ &= P_i\eta_i^n - (1-\theta)\Delta t \sum_{l=1}^{S_i} S_{i,l}\lambda_{j(i,l)} [(\Delta Z)^T U]_{j(i,l)}^n - \theta\Delta t \sum_{l=1}^{S_i} S_{i,l}\lambda_{j(i,l)} [(\Delta Z)^T A^{-1} \mathrm{G}]_{j(i,l)}^n \end{aligned} \tag{5-3}$$

Above Equation (5-3) has a strongly diagonally dominant, symmetric linear sparse matrix system of N_p equations for η_i^{n+1}, thus it can be efficiently solved by an iterative matrix solver, e.g., a preconditioned conjugate gradient method. Once the new water surface elevation at the center of each polygon is computed, substitute η_i^{n+1} into the momentum Equation (5-1), then we will get horizontal velocities at the new time level at each face, U_j^{n+1}. This Equation (5-1) has a tridiagonal system, and it can be solved efficiently by a direct tri-diagonal algorithm such as the Thomas Algorithm. Finally, the vertical component of the velocity can be obtained from the integration of the incompressible continuity Equation (2-4).

$$\begin{aligned} &w_{i,k+1/2}^{n+1} = w_{i,k-1/2}^{n+1} - \frac{1}{P_i} \sum_{l=1}^{S_i} S_{i,l}\lambda_{j(i,l)} \Delta z_{j(i,l),k}^n u_{j(i,l),k}^{n+1} \\ &k = m, m+1, \dots, M-1 \end{aligned} \tag{5-4}$$

5.2. Treatment of Flooding and Drying

Once the free surface elevation has been computed throughout the computational domain, before proceeding to the next time step, some of the vertical grid spacings $\Delta z_{j,k}^{n+1}$ must be updated to account for the new surface location. As shown in Figure 5-1, at each time step, the new total water depth at the polygon's sides, H_j^{n+1}, may be defined as

$$H_j^{n+1} = max\left[0\ (or\ dry\_depth), h_j + \eta_{i(j,1)}^{n+1}, h_j + \eta_{i(j,2)}^{n+1}\right] \tag{5-5}$$

According to the new total water depth, the vertical grid spacing Δz_j^{n+1} should be updated. Thus, an occurrence of zero value for the total water depth H_j^{n+1} implies that all the vertical faces separating prisms between the water column $i(j,1)$ and $i(j,2)$ are dry and may become wet at a later time when H_j^{n+1} becomes positive (Casulli and Walters, 2000). When the total depth is equal to zero, the friction factor at that point will be assumed to be infinity and, accordingly, the corresponding velocity u or v across the side of the cell forced to vanish. The occurrence of a zero value for the total depth in one side of a cell implies zero velocity or zero mass flux until the total depth becomes positive i.e., the boundary shorelines, which are varying with time, are defined by the condition of no mass flux. This guarantees mass conservation over the computational domain. An element is considered a dry cell only if the total water depths at all sides are zero.

To reduce computational noise or oscillation due to a very small wet element, a minimum critical dry depth is defined except using "0" in Equation (5-5). Therefore, elements are considered a wet element when the total water depth is greater than the critical depth and dry elements when the total water depth is less than or equal to the critical dry depth. The drying process can take place not only along the coast but also in interior regions such as shoals. For a shallow estuary, even under moderate wind stresses, some interior points over shoals can be dried completely whereas the surrounding elements are still wet. Similarly, when the sea surface elevation at a previously flooded location, that element returns to a dry cell. The unwanted numerical oscillation due to drying and wetting, such as the presence of a single wet or dry element surrounded by dry or wet elements, when the total water depth of a wet element drops below the specified threshold depth, drying occur, but an isolated dry element will not be turned into a wet cell until at least one of neighboring elements turns into a wet element as well.

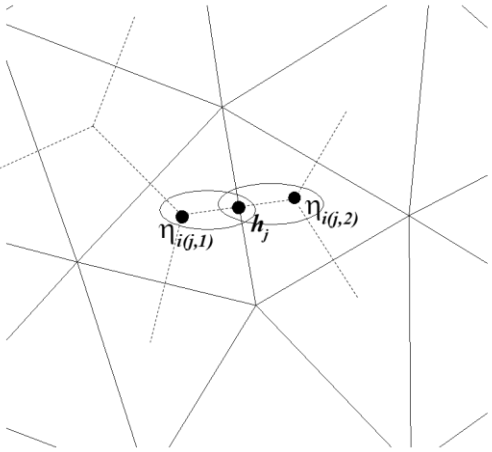

Figure 5-1. Determination of wet and dry depth at an element face.

6. Model Verification with Analytical Solutions

In previous sections, Sections 2 to 5, we showed governing equations, grid systems, numerical schemes, and solution algorithms used in GOM. These processes may be similar or

identical to other models, such listed by Fringer et al., 2019. However, conveying this information into a computer machine language is all different, and we used a standard FORTRAN 90 for this. Even though these processes are well-proven and robust approaches, any mistake in the final coding process leads to failure. To check the final success of this project, we compared a newly developed model, GOM, to well-known analytical solutions.

6.1. Wind Setup

The steady-state wind-induced setup due to constant wind stress in a rectangular basin can be written as

$$\eta(x) = \frac{\tau_w}{\rho g H}\left(x - \frac{L}{2}\right) \tag{6-1}$$

where η is the setup of the water surface, τ_w is the applied wind stress, H and L are the depth and length of the basin respectively, and the x is the distance from the origin. The horizontal grid used in the wind setup test is 21×5 cells with a length of 21 km and a width of 5 km. The depth of the computational domain is a constant 5 m, and the horizontal grid spacing is 1 km in both directions. Constant wind stress of 0.1 N/m^2 (i.e., 1 $dyne/cm^2$) is applied in the positive x-direction, and a time step of 30 seconds is used in the simulation. Both 2-dimensional (with one vertical layer) and 3-dimensional (with 5 vertical layers) setups are used to verify the model. Both analytical and numerical results are calculated/extracted from 0.5, 10.5, and 20.5 km from the origin and compared, and both 2D and 3D simulation results reached a steady-state condition in one day and are the same as the analytical results (Table 6-1 and Figure 6-1).

Table 6-1. Comparisons between analytical and simulated wind setup.

$x\ (km)$	$\eta_{analytical}(cm)$	$\eta_{2D\ model}(cm)$	$\eta_{3D\ model}(cm)$
0.5	-2.04	-2.04	-2.04
10.5	0	0	0
20.5	2.04	2.04	2.04

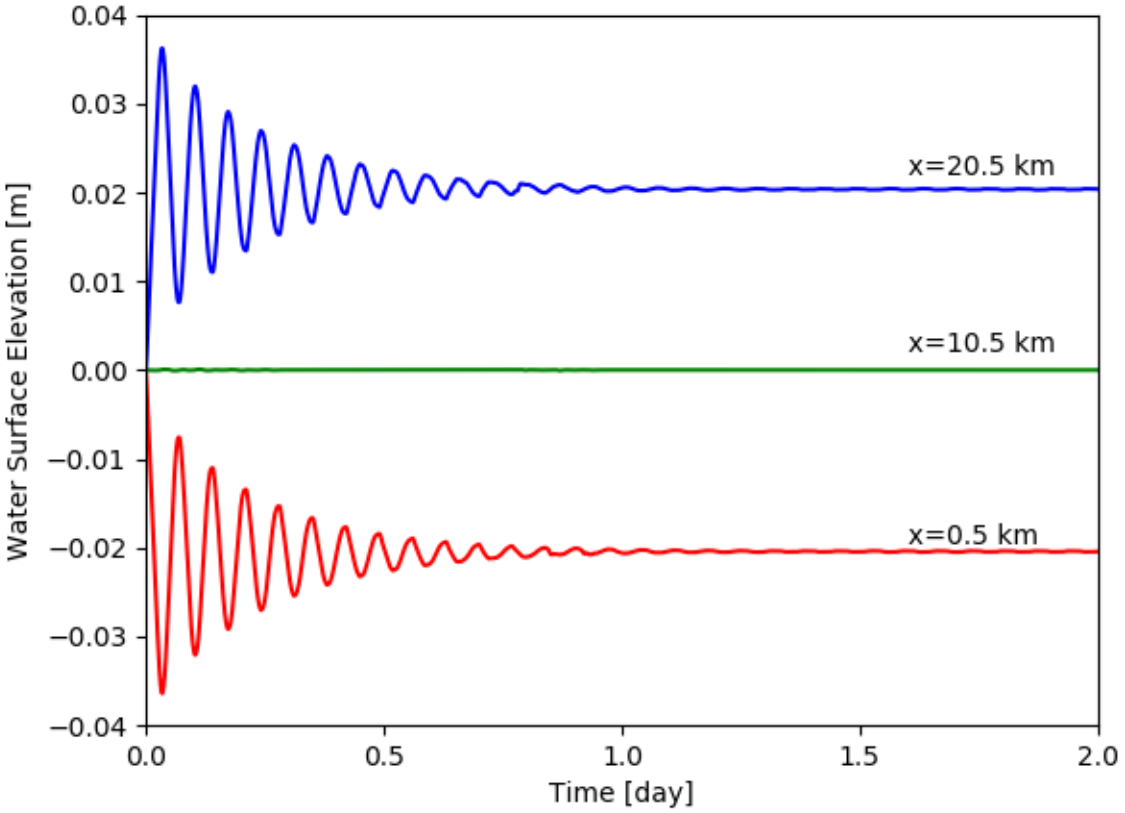

Figure 6-1. Comparison between analytical and numerical solutions of water surface elevation for wind setup test (2D simulation results).

6.2. Tidal Propagation with Constant Depth

Tide is the most significant phenomenon in the ocean, and thus tidal simulation is one of the most important applications of a coastal and estuarine hydrodynamic model. Lynch and Gray (1978) derived the analytical solutions for tidally forced estuaries of various geometries and depths. If we consider only tidal propagation term, i.e. the barotropic gradient term, in the original momentum Equation (2-1), and the continuity Equation (2-5), the one-dimensional shallow water equations in Cartesian coordinates are

$$\frac{\partial U}{\partial t} + gh\frac{\partial \eta}{\partial x} = 0 \tag{6-2}$$

$$\frac{\partial \eta}{\partial t} + \frac{\partial U}{\partial x} = 0 \tag{6-3}$$

where $U = uh$ is the depth-integrated velocity in x-direction. Assuming a closed boundary at $x = l$ and an open boundary at $x = 0$, the boundary conditions and initial conditions associated with Equations (6-2) and (6-3) are

Boundary conditions:

$$U(l,x) = 0$$

$$\eta(0,t) = \eta_0 + a \cdot \sin(\omega t) \tag{6-4}$$

Initial conditions:

$$\eta(x,0) = \eta_0$$

$$U(x,0) = 0$$

where a is a tidal amplitude, ω is an angular frequency of the given tide, η_0 is the initial water surface elevation measured from the undisturbed surface. With these initial and boundary conditions, the analytical solutions of the one-dimensional shallow wave equations for water surface elevation and velocity are (Liu, 1988)

$$\eta(x,t) = \frac{a \cdot \cos(k(l-x))}{\cos(kl)} \sin(\omega t) + \sum_{n=0}^{\infty} \left[\frac{-2a\omega}{lc(k_n^2 - k^2)} \sin(k_n x) \sin(\omega_n t) \right] + \eta_0 \tag{6-5}$$

$$U(x,t) = \frac{ac \cdot sin(k(l-x))}{\cos(kl)} \cos(\omega t) + \sum_{n=0}^{\infty} \left[\frac{-2a\omega}{l(k_n^2 - k^2)} \cos(k_n x) \cos(\omega_n t) \right] \tag{6-6}$$

where k is the wavenumber ($= \frac{2\pi}{L}$, where L is the wavelength), $k_n = \frac{(2n+1)\pi}{2L}$, l is the basin's length, n is the number of nodes, x is the interested location measured from the origin, and t is the time.

To compare the numerical solution with a linear analytical solution, a rectangular basin with a constant water depth of 10 meters is considered. The model domain is discretized with 929 mixed elements (quadrilateral elements at the left and triangular elements at the right, $\Delta x = \Delta y = \sim 2km$) and one vertical layer as shown in Figure 6-2; note that the only reason we constructed a mixed grid in this problem was to prove our model's capability to handle both triangular and rectangular grids. Input tidal forcing along the open boundary was set with 0.5 m of amplitude and a period of 12.42 hours. The simulation time step was set to 30 minutes, and the test simulations were run with $\theta = 1$ and $\theta = 0.5$, respectively. It is noted that when using the implicit numerical scheme, i.e. $\theta = 1$, numerical diffusion is introduced. Thus, the numerical solution should correspond to the first mode of the analytical solution, which corresponding to the first terms of Equations (6-5) and (6-6). If a semi-implicit scheme, i.e. $\theta = 0.5$, is used the numerical solution should be compared to the complete Equations (6-5) and (6-6) which include the higher mode solution (Liu, 1988; Lee, 2008).

The model results were extracted from three locations and compared with analytical solutions: (1) near the mouth (Station 1, $x = 9\ km$, $y = 15\ km$), (2) middle of the basin (Station 2, $x = \sim 29.1\ km$, $y = \sim 14.7\ km$), and (3) near the closed boundary (Station 3, $x = \sim 50.7\ km$, $y = \sim 14.7\ km$). Model results with $\theta = 1$, which should be compared with the first term in the analytical solution, agree well with analytical solutions (Figure 6-3). When $\theta = 0.5$ is used, which should be compared with the full equation, the model results had a little discrepancy with analytical solutions but mostly agrees well (Figure 6-4).

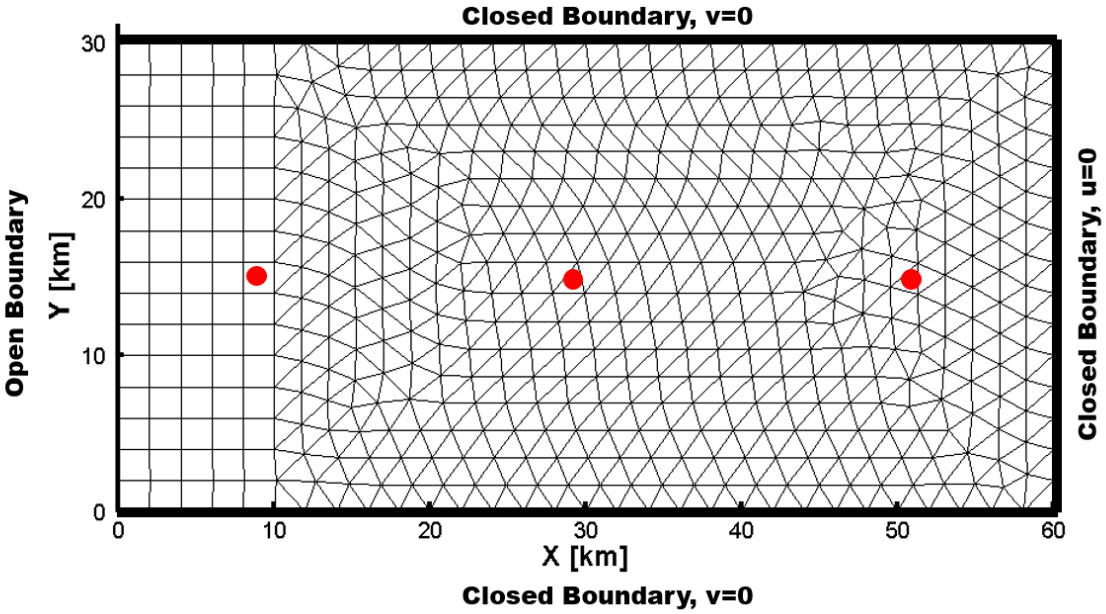

Figure 6-2. Computation domain and mixed (quadrilateral and triangular) meshes for tidal propagation tests. Three red dots denote the model simulation comparison location, from the left to the right - station 1, 2, 3.

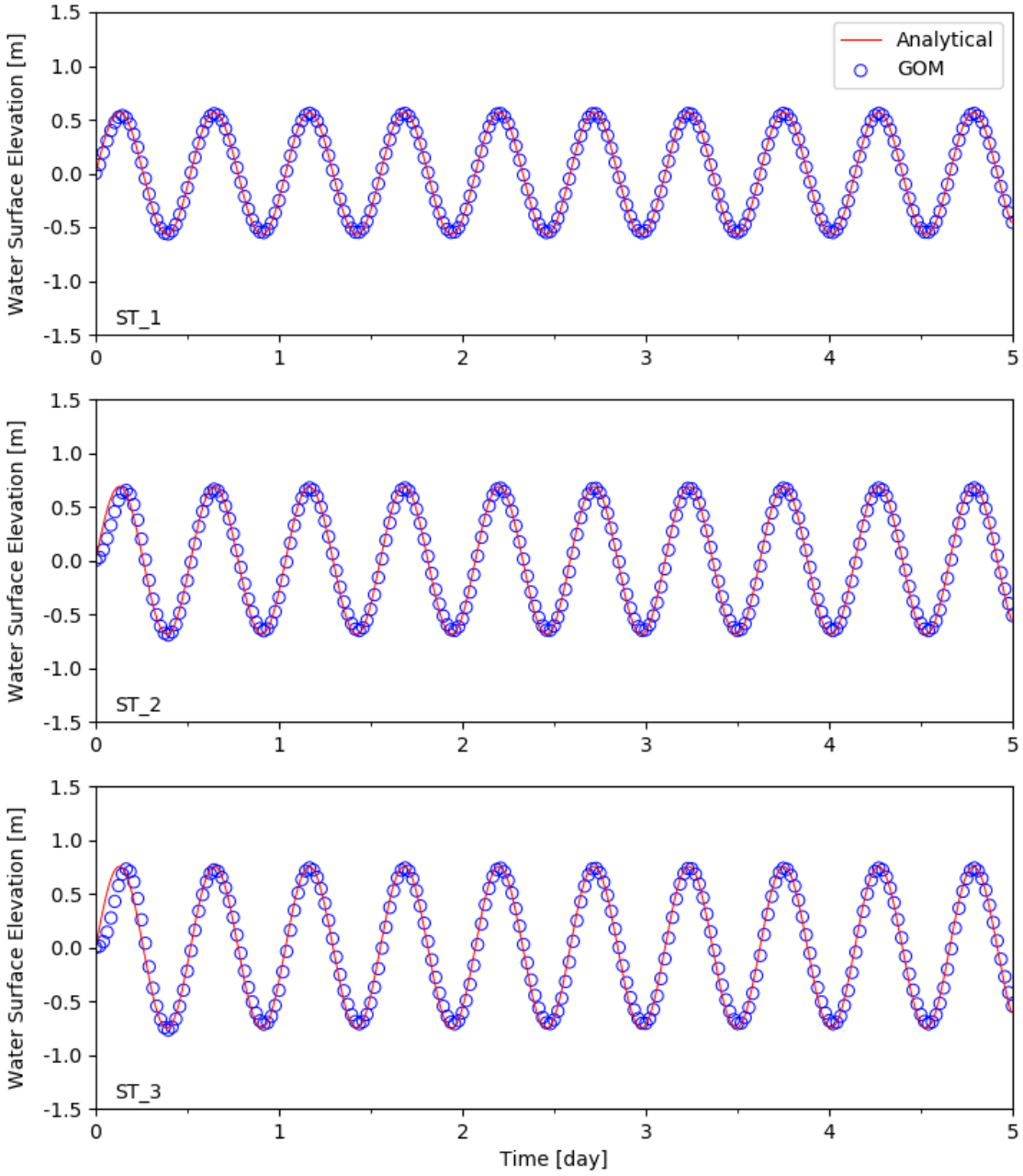

Figure6-3. Comparison of water surface elevation for tidal propagation test at three different locations with $\theta = 1.0$. Solid lines and circles represent analytical solutions and numerical results, respectively.

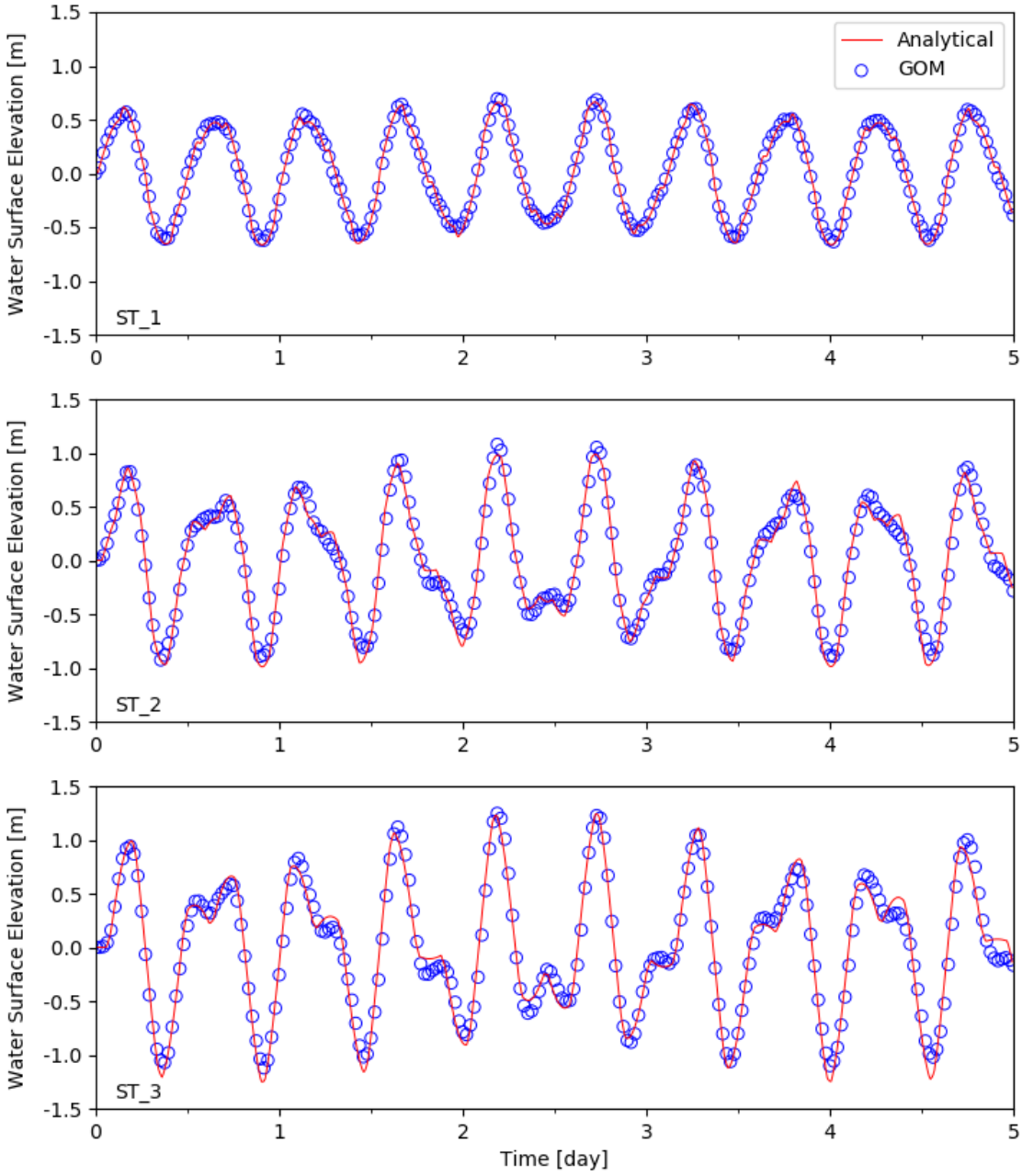

Figure 6-4. Comparison of water surface elevation for tidal propagation test at three different locations with $\theta = 0.5$. Solid lines and circles represent analytical solutions and numerical results, respectively.

6.3. Tidal Propagation with Non-Linear Advection

If nonlinear advection terms are included in the two-dimensional shallow water equations, it is not feasible to obtain an analytical solution. However, if the equations are reduced to one-dimension, we can obtain the harmonic series solution. Including only non-linear advection and propagation terms, the original momentum Equation (2-1) and the continuity Equation (2-5) can be reduced as

$$\frac{\partial U}{\partial t} + \frac{\partial uU}{\partial x} + gh\frac{\partial \eta}{\partial x} = 0 \tag{6-7}$$

$$\frac{\partial \eta}{\partial t} + \frac{\partial U}{\partial x} = 0 \tag{6-8}$$

The boundary conditions are

$$\begin{aligned} u(l,t) &= 0 \\ \eta(0,t) &= a \cdot \sin(\omega t) \end{aligned} \tag{6-9}$$

With the boundary conditions, the analytical solution of Equations (6-7) and (6-8) up to the first order can be written as (Liu, 1988)

$$\begin{aligned} \eta(x,t) = {} & \frac{a\cos(k(l-x))}{\cos(kl)}\sin(\omega t) \\ & + \frac{a^2 k}{8h\cos^2(kl)}\left[x\sin\big(2k(l-x)\big) + \frac{l}{\cos(4kl)}\sin(2k(l+x))\right. \\ & \left. - \frac{l}{\cos(4kl)}\tan(2kl)\cos(2x(l-x))\right]\cos(2\omega t) \end{aligned} \tag{6-10}$$

$$\begin{aligned} u(x,t) = \frac{1}{h}\Bigg[& \frac{ac\sin(k(l-x))}{\cos(kl)}\cos(\omega t) \\ & + \frac{a^2 k}{8h\cos^2(kl)}\left[x\cos\big(2k(l-x)\big) + \frac{l}{2k}\sin(2k(l-x))\right. \\ & - \frac{l}{\cos(4kl)}\cos(2k(l+x)) \\ & \left. + \frac{l}{\cos(4kl)}\tan(2kl)\sin(2k(l-x))\right]\sin(2\omega t)\Bigg] \end{aligned} \tag{6-11}$$

To test non-linear advection term in the developed model, numerical simulations were conducted with the identical basin and tidal forcing conditions used in the previous test. Because the analytical solutions present up to the first mode solution, the implicit numerical solution, $\theta = 1$, should be compared to the analytical solution. Numerical results were extracted at the

same three locations as in the previous test (Figure 6-2) and compared with analytical solutions. The results show that the numerical and analytical solutions are in good agreement (Figure 6-5).

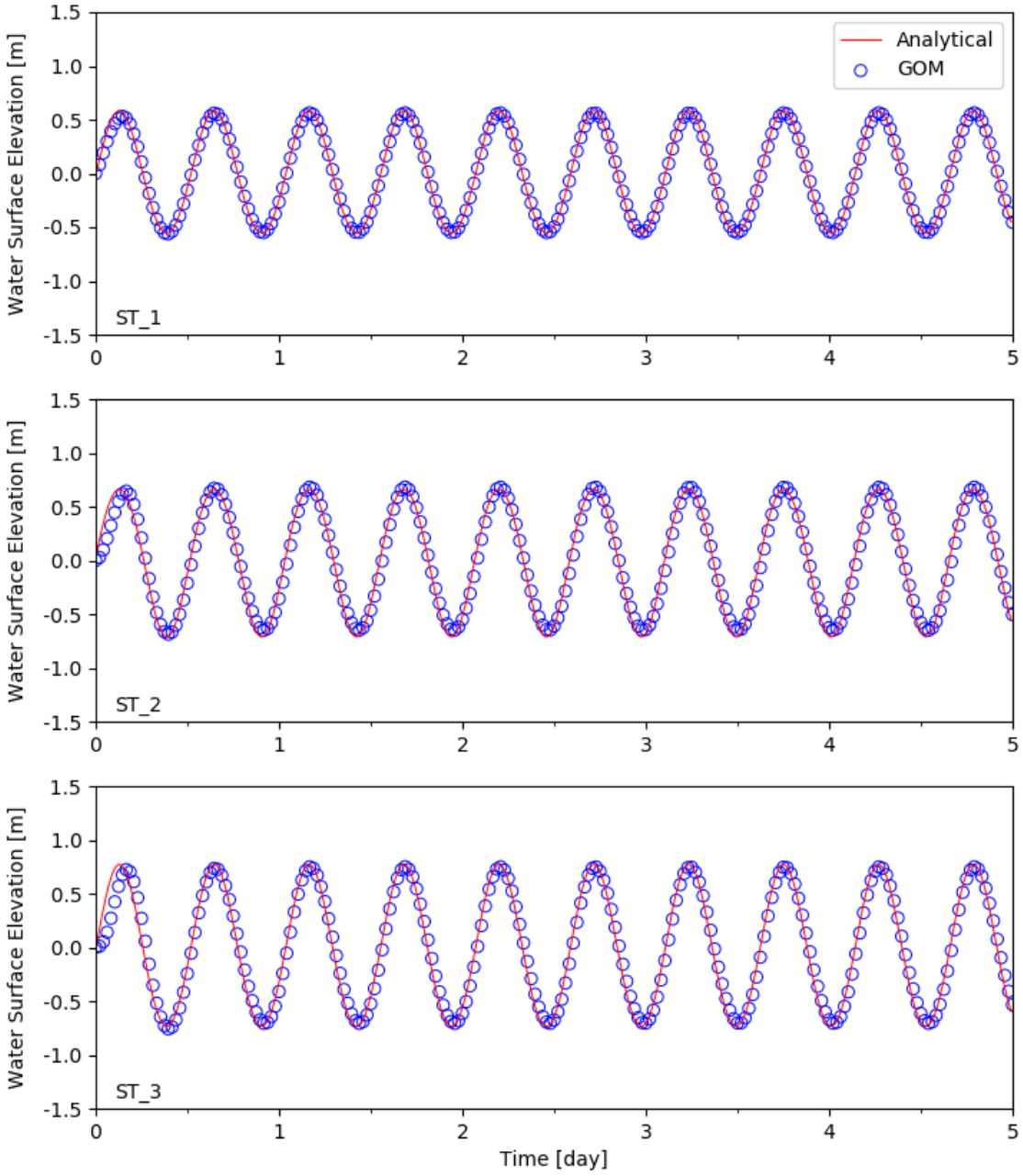

Figure 6-5. Comparison of water surface elevation for non-linear advection at three different locations with θ=1.0. Solid lines and circles represent analytical solutions and numerical results, respectively.

6.4. Quarter-Annular Harbor Test with a Sloping Bottom

Lynch and Gray (1978) derived the analytical solutions for a tidally forced estuary with a flat bottom and a sloping bottom. The quarter-annular test, which contains spatially varying geometry and bathymetry, is one of the well-known test cases for testing the integrated numerical schemes of a developed ocean circulation numerical model. Numerical results will be poor with spurious oscillations or with excessive numerical dissipation if poor numerical schemes are used.

The analytical solutions for the Quarter-annular harbor test are well described by Lynch and Gray (1978) and Lynch and Officer (1985). Neglecting nonlinear, Coriolis, and horizontal diffusion terms and assuming linear bottom friction, we can obtain the following vertically averaged equations

$$\frac{\partial u}{\partial t} + g\frac{\partial \eta}{\partial x} + \tau u = 0 \tag{6-12}$$

$$\frac{\partial v}{\partial t} + g\frac{\partial \eta}{\partial y} + \tau v = 0 \tag{6-13}$$

$$\frac{\partial \eta}{\partial t} + \frac{\partial hu}{\partial x} + \frac{\partial hv}{\partial y} = 0 \tag{6-14}$$

where η is water surface elevation, u and v are vertically averaged velocities, g is gravitational acceleration, and τ is the linear bottom friction coefficient. With the following boundary conditions: no flow boundaries at the closed end, $r = r_1$ which is the inner radius for the quarter-annular harbor, at the open boundary, $r = r_0$ which is the outer radius for the quarter-annular harbor, periodic tidal forcing $\eta = \eta_0 \cos(\omega t)$, where η_0 is amplitude, the analytic solutions for surface elevation and horizontal velocity are (Lynch and Gray, 1978; Lynch and Officer, 1985)

$$\eta(r,t) = Re\left\{(Ar^{s_1} + Br^{s_2})e^{i\omega t}\right\} \tag{6-15}$$

$$v(r,t) = Re\left\{(As_1 r^{s_1-1} + Bs_2 r^{s_2-1})\frac{i\omega}{\beta^2 H_0}e^{i\omega t}\right\} \tag{6-16}$$

where

$$A = \frac{\eta_0 s_2 r_1^{s_2}}{s_2 r_1^{s_2} r_2^{s_1} - s_1 r_1^{s_1} r_2^{s_2}}, \qquad B = \frac{-\eta_0 s_1 r_1^{s_1}}{s_2 r_1^{s_2} r_2^{s_1} - s_1 r_1^{s_1} r_2^{s_2}}$$
$$s_1 = -1 + \sqrt{1-\beta^2}, \qquad s_2 = -1 - \sqrt{1-\beta^2} \tag{6-17}$$
$$\beta^2 = \frac{(\omega^2 - i\omega\tau)}{gh_0}, \qquad h_0 = \frac{h_1}{r_1^2}$$

$$\tau = \frac{N}{h^2}\left[\frac{\lambda^2 \tanh(\lambda)}{\lambda + \left(\frac{\lambda^2}{K} - 1\right)\tanh(\lambda)}\right]$$

$$K = \frac{kh}{N}, \qquad \lambda = \sqrt{\frac{i\omega h^2}{N}}$$

and N is the eddy viscosity; k is the bottom friction.

The tested computational domain consists of a quarter of an annulus enclosed with land boundaries on three sides and an open ocean boundary on the outer edge. The inner radius has $r_1 = 60{,}960\ m$ $(= 200{,}000\ ft)$, and the outer radius has $r_0 = 152{,}400\ m$ $(= 500{,}000\ ft)$. The bathymetry along the inner radius r_1, is $h_1 = 3.048\ m$ $(= 10\ ft)$, and it drops quadratically at radius r (Luettich et al., 2002), i.e. $h_r = h_1 r^2 / r_1^2$. The discretization uses a radial spacing of $15{,}240\ m$ $(= 50{,}000\ ft)$ and an angular spacing of 11.25 degrees. Then, the computational domain consists of 48 rectangular cells with 63 nodes (Figure 6-6).

The model started from a state of rest, and periodic tidal force at the open boundary, advection, and quadratic bottom friction terms are activated. The elevation boundary is forced with a spatially uniform M_2 tide (tidal period = 12.42 hrs) with amplitude of 0.3048 m $(= 1\ ft)$. Total simulation time was set to 5 days with a time step of 174.656 seconds. Modeled water level time series are extracted every time step at 3 different locations in the domain, and the numerical results showed a good agreement with analytical solutions (Figure 6-6).

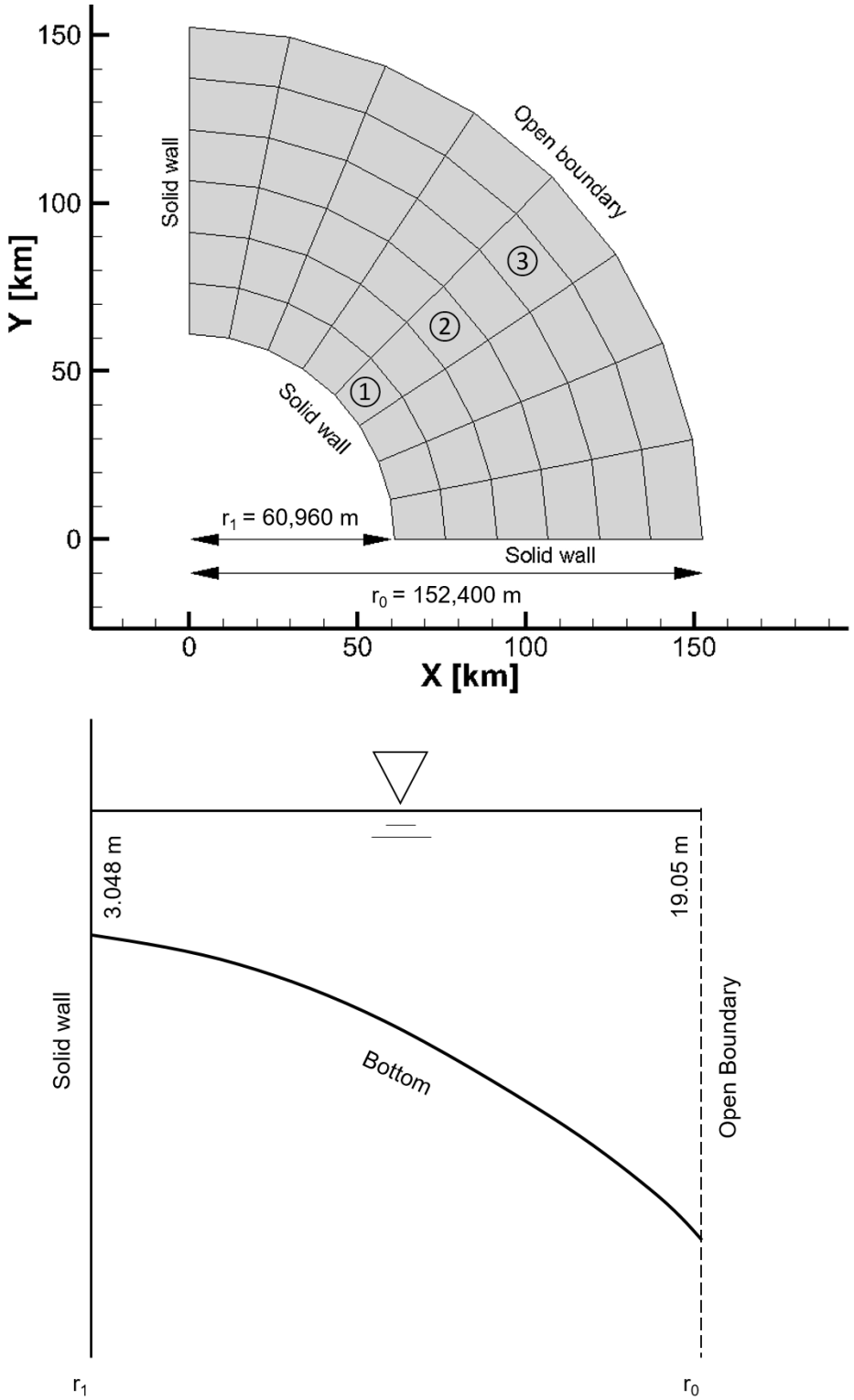

Figure 6-6. Computational mesh for the quarter annular test. Upper panel: x-y plane, lower pannel: x-z plane. Three data extraction stations are shown with numbers on the upper panel.

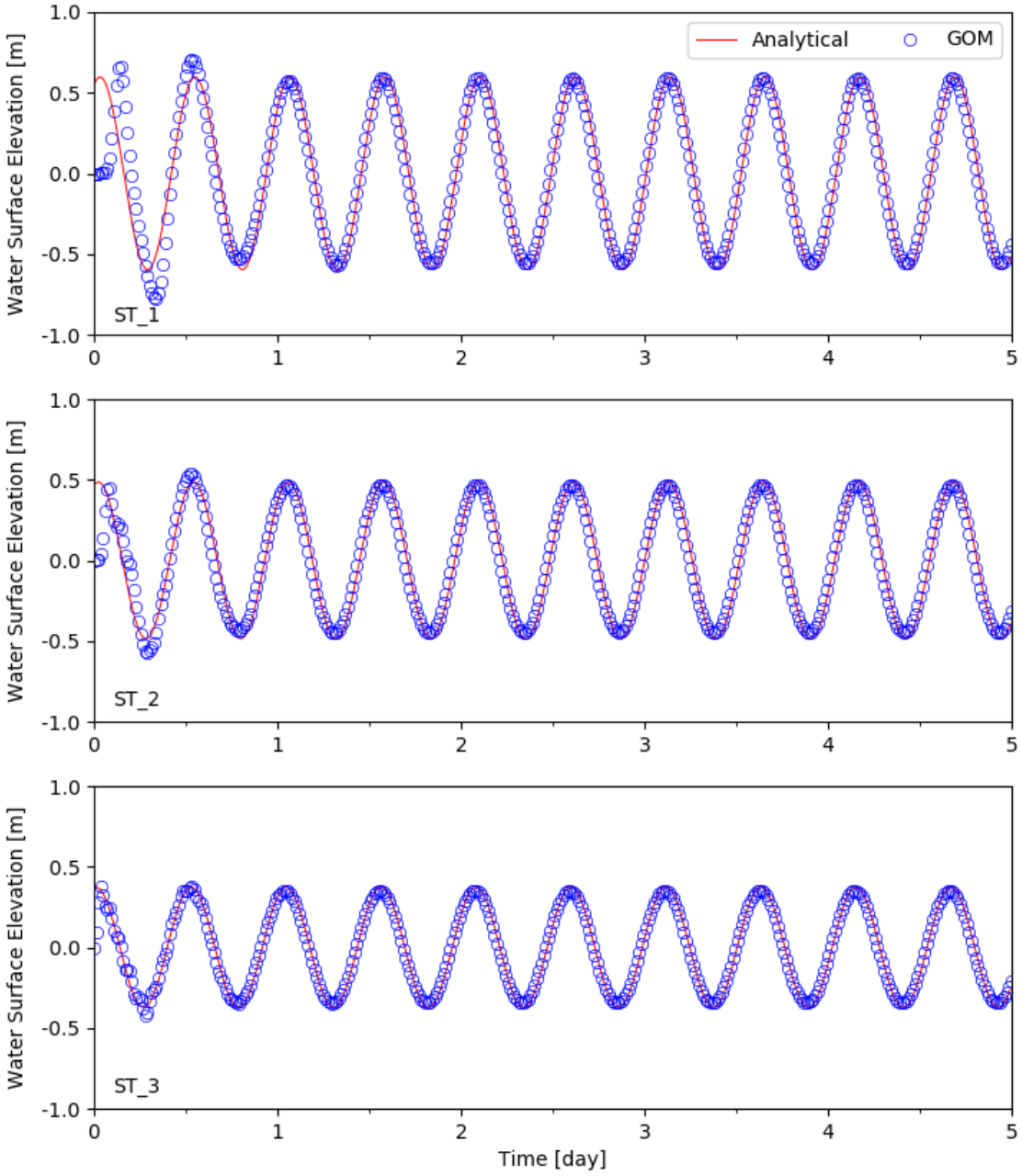

509

510 Figure 6-7. Comparison of water surface elevation for the Quarter Annular test case at three
511 different locations. Solid lines and circles represent analytical solutions and numerical results,
512 respectively. ST_1, ST_2, and ST_3 denote results extraction locations as in Figure 6-6,
513 respectively.
514

6.5. Wetting and Drying Test over Tidal Flats

Some shallow parts of coastal water bodies become wet and dry periodically responding to the tide, and thus the correct reproduction of the wetting and drying of the tidal flats is one of the desirable features of numerical tidal flow models based on shallow water equations. There are many different approaches to solve the wetting and drying process, and the major difference between all the models is the way to determine the drying and wetting cells and depths. The method to determine drying cells in the present model is based on Casulli and Walters (2000), as explained in Equation (5-5).

To validate the wetting and drying scheme implemented in the developed model, we compared our model results with the analytical solution developed by Carrier and Greenspan (1958). The derivation of the analytical solution is well-reviewed in several papers (e.g., Liu, 1998; Sobey, 2009; Mungkasi and Roberts, 2012). To compare with the analytical solution, a rectangular basin with a linearly sloping bottom is considered. The length and the width of the basin are set to 55 km and 100 m, respectively. The water depth at the origin, $x = 0$ m, is set to 50 m, and the bottom slope, α, is 1:1000; thus, the initial land and water interface is at $x = 50$ km (Figure 6-8). The computational domain is divided by 550×1 quadrilateral elements ($\Delta x, \Delta y = 100\ m$). A periodic tide with an amplitude 0.2 m and a period of 1 hour is applied at the open boundary, at $x = 0$ m. Analytical results, which are originally given with non-dimensional variables, are converted to dimensional variables and compared with model results. Both analytical and numerical results are calculated and extracted every $\frac{1}{6}\pi$ tidal period and compared. Numerical simulation results show that the analytical and the numerical solutions are in good agreement showing that the wetting and drying process implemented in GOM works well (Figure 6-9 and Figure 6-10).

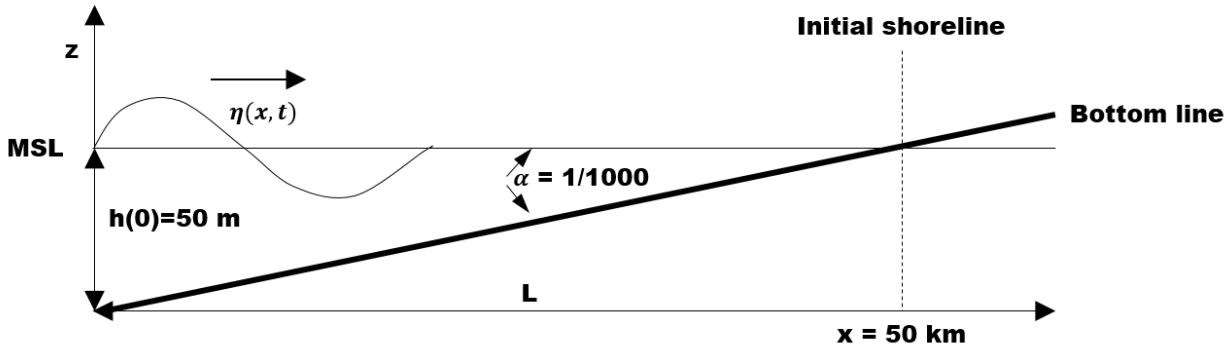

Figure 6-8. Definition sketch for Carrier and Greenspan (1958) analytical solution on a linearly sloping beach.

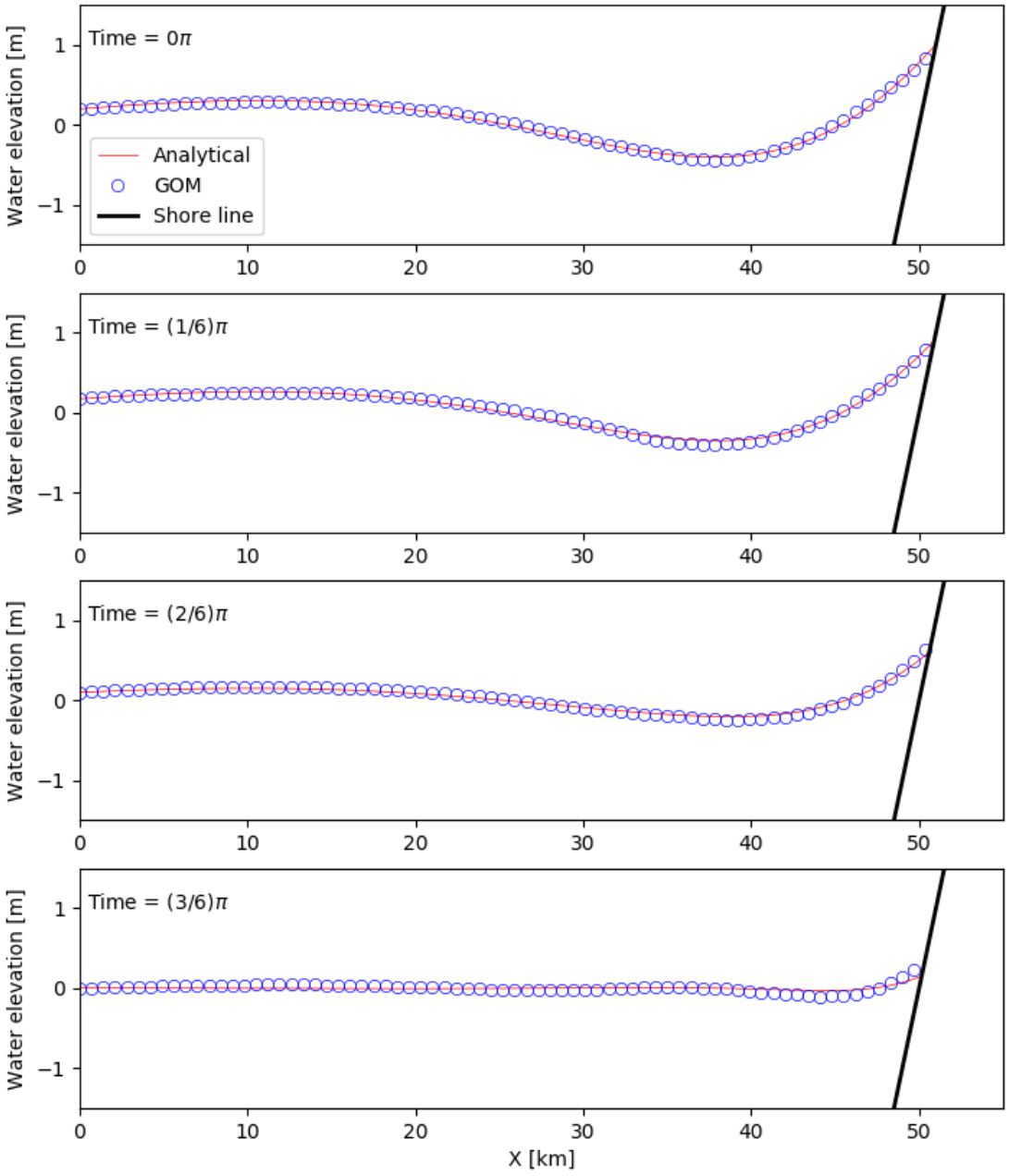

543

544 Figure 6-9. Comparison of wave profiles as predicted by theory (solid red lines) and numerical
545 model (blue circles) of wetting and drying at time = 0 to $\pi/2$.

546

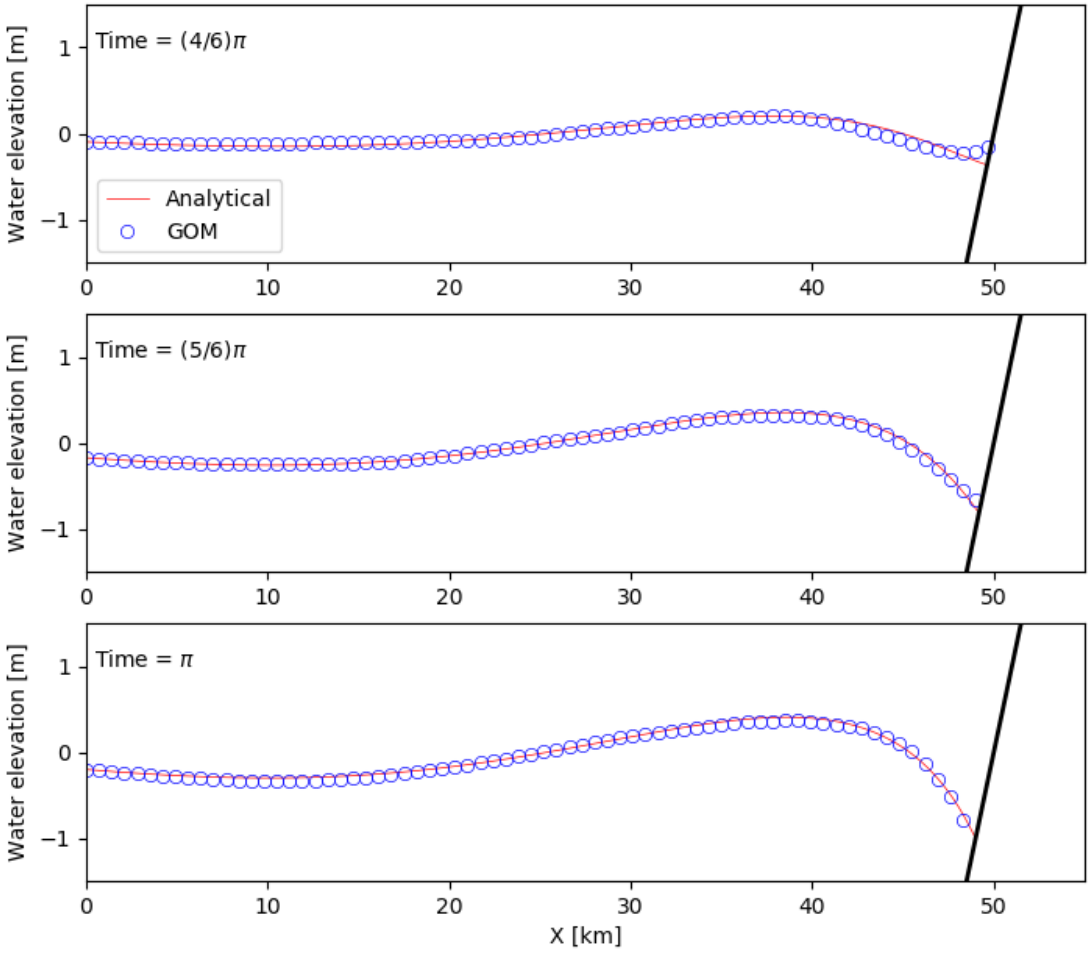

Figure 6-10. Comparison of wave profiles as predicted by theory (solid red lines) and numerical model (blue circles) of wetting and drying at time = 2π/3 to π.

7. Model Application to the Texas Coast

Even though a model is verified with some analytical problems, it is sometimes not enough since each analytical problem is focused only on a specific term. For this reason, it is also important to verify the model with a realistic field problem which includes all the physical aspects. The developed model, GOM, is applied to highly complex geometry, the northern Texas coast, to assess the performance of the developed model. Then, the model results are compared with the results of one of the well-known and widely used ocean circulation models, the Semi-Implicit Cross-Scale Hydroscience Integrated System Model (SCHISM).

7.1. Model Domain and Grid Generation

We developed a model grid from the lower Galveston Bay to Sabine Lake (Figure 7-1). We used 'National Oceanic Atmospheric Administration (NOAA) Medium Shoreline' data for the land/sea boundary and 'Coastal Bathymetry 2013' from the 'Texas Natural Resources

Information System (TNRIS)' to correctly identify the locations of ship channels and the Intracoastal Waterway. The horizontal grid resolution varies from about 10 meters at ship channels to about 3,000 meters at offshore boundaries. Most of the ship channels are resolved with rectilinear elements, and otherwise, most of the model domains are covered by triangular elements. The offshore boundary for the model domain was set at about 15 kilometers offshore from the coastline, and the final horizontal grids consist of 210,510 elements and 126,474 nodes.

After the horizontal grid was generated, the digital elevation models (DEMs) were interpolated onto the computational grid using the Inverse Distance Weight (IDW) interpolation method. We used two different sources of DEMs: (1) ETOPO1 Global Relief Model, and (2) Coastal Relief Model (CRM). The ETOPO1 is a 1 arc-minute global relief model of Earth's surface that integrates land topography and ocean bathymetry, and it covers the entire Gulf of Mexico. The CRM has finer spatial resolution than ETOPO1; it provides one of the 3 arc-seconds, 1/3 arc-seconds, and 1/9 arc-seconds resolution DEM depending on the area. Some portions of the study area are covered by either 1/3 or 1/9 arc-seconds DEM, thus both data are interpolated onto the grid; note that the minimum water depth was set to 1.0 m throughout the model domain.

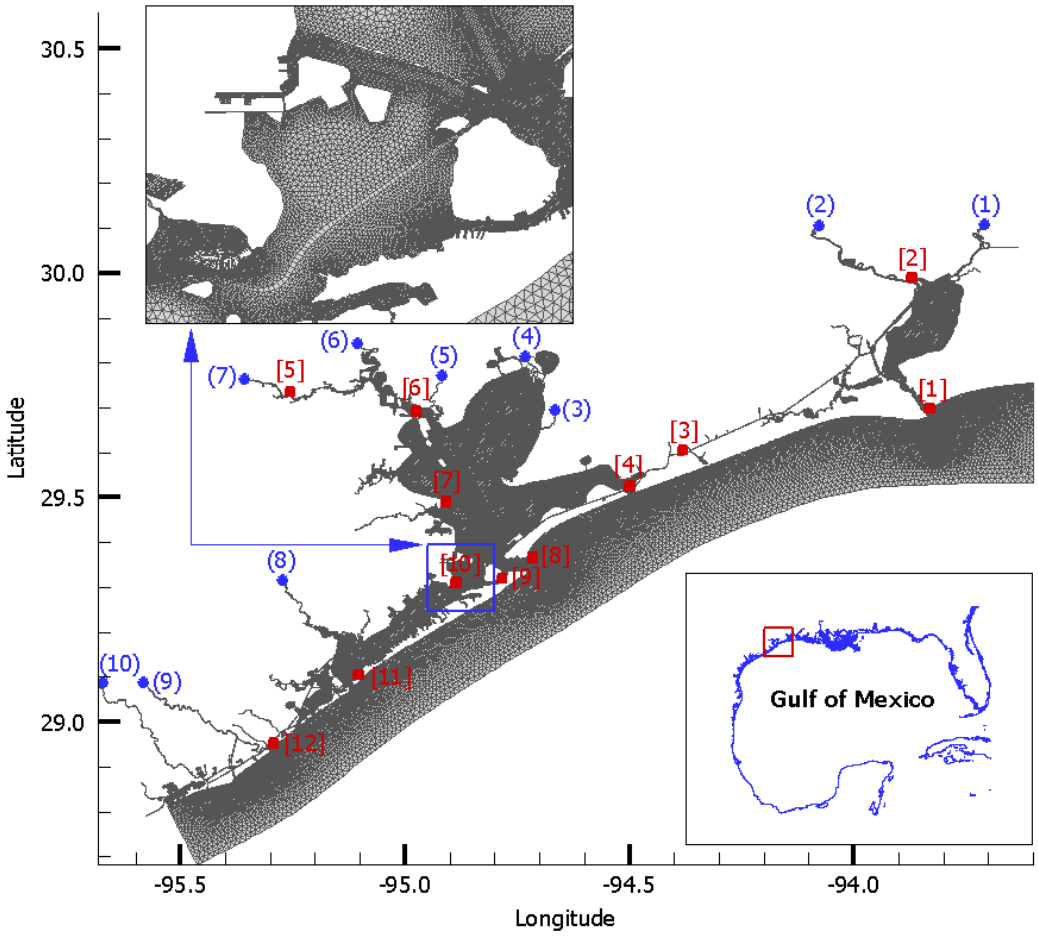

Figure 7-1. The model domain and the horizontal grid. The ten blue dots denote included river boundaries, and the twelve red squares show NOAA tide stations; the numbers are the corresponding station numbers in Table 7-1. The upper panel is the zoom-ins of the selected coastal area at the lower Galveston Bay.

7.2. Forcing conditions and model setup

The developed model was validated for the one-month period in July 2017 and was forced by the tides, river discharge, and atmospheric wind stress. Three NOAA tide stations data, which are relatively close to the open boundary grids, were interpolated to the model boundary grids: Freeport (NOAA 8772447), Galveston Bay Entrance (NOAA 8771341), and Sabine Pass (NOAA 8770822) (Figure 7-1 and Table 7-1). Daily freshwater inflows obtained from the United States Geological Survey (USGS) gaging stations were specified at 10 river boundaries (Figure 7-1 and Table 7-1). These USGS stations are mostly located several kilometers upstream from the model river boundary nodes, but we assumed that there were no additional sources and sinks between the river gages and model river boundary nodes. For the wind stress, the North

595 American Mesoscale forecast system (NAM) 6 hourly reanalysis data was interpolated onto the
596 entire horizontal model grids. Spatially uniform bottom friction with Manning's coefficient of
597 0.016 was used.

598 The still water condition was considered at the beginning, i.e., no water surface elevation
599 disturbance and no water movement. The Implicitness parameter was set to 0.6, and a two-
600 dimensional simulation was considered. Finally, the model simulation time step was set to 600
601 seconds. Note that we also ran the SCHISM model with identical model setups to compare the
602 simulation results.
603

604 Table 7-1. NOAA tide stations and USGS river gaging stations used in the model simulation.

# in Figure 7-1	NOAA Station ID	Station Name	USGS Station ID	Station Name
1	8770822	Sabine Pass	08030500	Sabine River
2	8770520	Rainbow Bridge	08041780	Neches River
3	8770808	High Island	08042558	Double Bayou
4	8770971	Rollover Pass	08067070	Trinity River
5	8770777	Manchester	08067500	Cedar Bayou
6	8770613	Morgans Point	08070200	San Jacinto River
7	8771013	Eagle Point	08074500	Buffalo Bayou
8	8771341	Galveston Bay Entrance	08078000	Chocolate Bayou
9	8771450	Galveston Pier 21	08116650	Brazos River
10	8771486	Galveston Railroad Br.	08117705	San Bernard River
11	8771972	San Luis Pass	-	-
12	8772447	Freeport	-	-

605

606 7.3. Model validation

607 Model simulation results of the developed model, GOM, and the SCHISM were
608 compared with the hourly measured water surface elevation data at twelve NOAA tide stations
609 which are shown in Figure 7-1 and Table 7-1. Figure 7-2 and Figure 7-3 show that the results of
610 both models are almost identical and give a good agreement with observed water surface
611 elevations. Note that there are some differences at the beginning of the simulation, but that was
612 caused by applying a tide ramping up option only for SCHISM simulation.

613 To better evaluate the model simulation results, we used two types of quantitative error
614 analysis methods: Mean Absolute Error (MAE), and Predictive Skill (it is also called Skill or
615 Index of Agreement) which was introduced by Willmott (1982). They are defined as follows
616 (Kim and Park, 2012; Lee et al., 2017):

$$MAE = \frac{\sum|M_n - O_n|}{N} \tag{7-1}$$

$$Skill = 1 - \frac{\sum(M_n - O_n)^2}{\sum(|M_n - \bar{O}| + |O_n - \bar{O}|)^2}, \qquad (0 \le Skill \le 1) \tag{7-2}$$

where M_n and O_n are nth modeled and observed data, respectively; N is the total data number compared, and $\bar{O}$ is the mean observed value. The mean absolute error explains how much the modeled data deviates from the observed data, and the value of Skill explains how much the model can reproduce the observed data, and the value '*Skill* = 1' indicating the perfect agreement (Lee et. al., 2017).

When performing the error analysis, the first 5-day simulation results were excluded since the model required times to be stabilized. Overall, the developed model reproduces water surface elevations well throughout the entire model domain, and the results are quite similar to the SHSIM (Table 7-2). The overall MAE is 5.6 cm for the GOM simulation, varying from 2.1 cm to 10.5 cm. The model Skill value varies from 0.887 to 0.995, and the overall value is 0.951 indicating the developed model performs well in a complex geometric study area with realistic forcing conditions. Note that there are some possibilities we can improve the model simulation results modulating bathymetry, bottom friction, and tidal boundary conditions. Applying spatially varying bottom friction is a common remedy to increase the model simulation results, and it is better to apply the correctness factors for the tidal amplitude and phase when the reference tide stations are off from the model's boundary nodes. However, we ignored them since the goal of this simulation was not the improving model simulation results but the validating the developed model's performance.

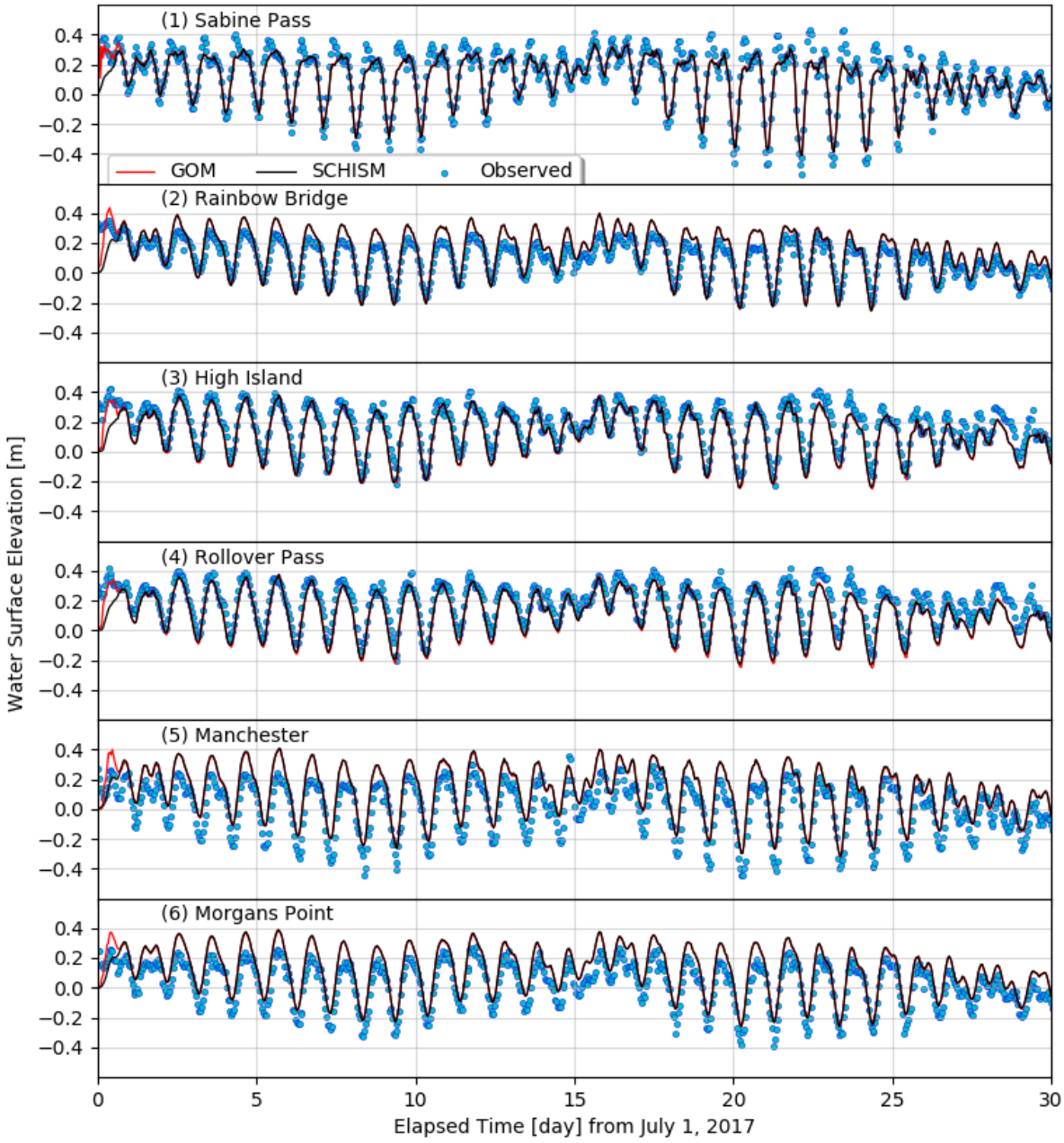

Figure 7-2. Water surface elevation comparison between measured (blue circles), GOM simulation results (solid red lines), and SCHISM simulation results (solid black lines), from station 1 to 6.

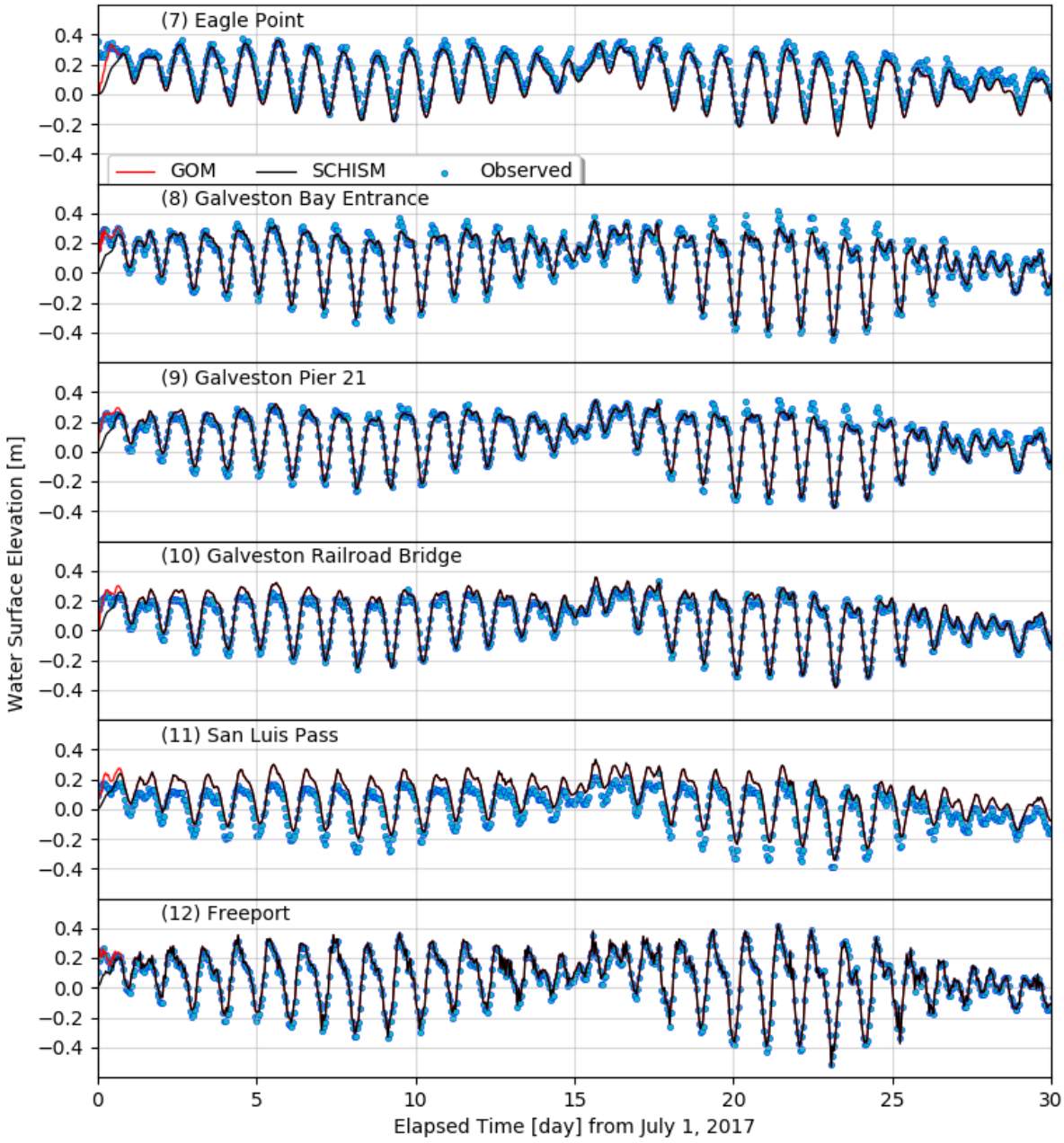

639

640 Figure 7-3. Water surface elevation comparison between measured (blue circles), GOM
641 simulation results (solid red lines), and SCHISM simulation results (solid black lines), from
642 station 7 to 12.
643

644 Table 7-2. Error analysis of the surface elevation simulation, both for the SCHISM and GOM.

Tide station	SCHISM	GOM	N

	MAE (cm)	Skill	MAE (cm)	Skill	
(1) Sabine Pass	5.4	0.959	5.3	0.961	600
(2) Rainbow Bridge	5.5	0.945	5.5	0.945	600
(3) High Island	5.5	0.951	5.6	0.950	600
(4) Rollover Pass	6.4	0.934	6.5	0.931	600
(5) Manchester	10.8	0.897	10.5	0.901	600
(6) Morgans Point	9.1	0.909	8.8	0.912	600
(7) Eagle Point	5.0	0.957	5.1	0.955	600
(8) Galveston Bay Entrance	3.6	0.984	3.6	0.983	600
(9) Galveston Pier 21	3.2	0.981	3.3	0.980	600
(10) Galveston Railroad Br.	3.2	0.984	3.2	0.983	600
(11) San Luis Pass	8.1	0.890	8.1	0.887	600
(12) Freeport	2.2	0.994	2.1	0.995	600
Overall	5.7	0.951	5.6	0.951	7200

8. Conclusions

We developed a three-dimensional numerical model with an orthogonal unstructured grid, either triangular or quadrilateral, for coastal and estuarine circulation, which we named as the General Ocean Model (GOM). This model is implemented with a combined finite difference and finite volume method. To eliminate the major simulation time step constraint which arises when solving shallow water equations, we used a semi-implicit method, which is stable when the implicitness factor, θ, is between 0.5 and 1.0, for wave propagation term. To moderate another time constraint, we adopted the Eulerian-Lagrangian Method for the non-linear advection term. In addition to the elimination of time constraints, exact numerical conservation is achieved by using the finite volume method.

We benchmarked an algorithm developed by Casulli and Walters (2000), and this algorithm is simple, stable, and efficient. The algorithm is easy to expand from 2D to 3D equations, and by implementing ELM and semi-implicit schemes this model can be used with fine spatial and vertical resolutions of the grid with relatively large time steps. We aimed to develop a model that can be used in coastal and estuarine regions, and thus the wetting and drying process is naturally achieved. In addition, this model can be used for a storm surge simulation since the atmospheric pressure term is included.

The developed model, GOM, was successfully passed five analytical tests we chose, and finally verified with a realistic application to the Texas coast. The model simulation results were also compared with one of the well-known and widely used ocean circulation models, SCHISM, to double-check the model performance. Even though this model is successfully tested, there are some aspects we want to improve our model comparing to well-recognized ocean circulation models, which mentioned by Fringer et al. (2019). With the Z-grid system, which the current version of our model uses, the model saved computational time in 3-dimensional simulations because the number of vertical grid cells is less in the shallow water area. However, the model requires one big surface layer, and this unwillingly reduces 3D to 2D in shallow water or inundation area, thus it is difficult to resolve 3D motions in the shallow area; this drawback will

673 be improved by implementing sigma (σ) grid. Another missing puzzle in this model, which aims
674 to solve general coastal water motions, is the missing of transport equations. Even though this
675 model includes the baroclinic gradient term, salinity transport equation is not yet included.
676 Implementation of these in this model will be our next task.

677

678

Acknowledgments

The authors would like to especially thank Dr. Seog-Ku Kim for the support for the project initiation and useful discussions throughout the project. This work was supported by the Korea Institute of Civil Engineering and Building Technology (KICT) (project number: 20150121-0001-01) and the National Research Council of Science & Technology (NST) granted by the Korea Government (MSIT) (No. CAP-18-07-KICT). The NOAA Medium Shoreline data is available at https://shoreline.noaa.gov/data/datasheets/medres.html. The 'Coastal Bathymetry 2013' is available from TNRIS: https://data.tnris.org/collection/8fe992d8-1019-492a-b36b-9cfc3293ac6b. The ETOPO1 Global Relief Model is available at https://data.nodc.noaa.gov/cgi-bin/iso?id=gov.noaa.ngdc.mgg.dem:316. The Coastal Relief Model (CRM) is available at https://www.ngdc.noaa.gov/mgg/coastal/crm.html. The North American Mesoscale forecast system (NAM) reanalysis data was downloaded from https://www.ncdc.noaa.gov/data-access/model-data/model-datasets/north-american-mesoscale-forecast-system-nam#targetText=The%20North%20American%20Mesoscale%20Forecast,NCEP)%20for%20producing%20weather%20forecasts.&targetText=The%20NAM%20generates%20multiple%20grids,continent%20at%20various%20horizontal%20resolutions. The USGS gaging station data is available at https://maps.waterdata.usgs.gov/mapper/index.html. The model, GOM, simulation results for the Texas coast case can be downloaded from the Mendeley Data (archiving is underway).

References

Carrier, G. F., & Greenspan, H. P. (1958). Water waves of finite amplitude on a sloping beach. *Journal of Fluid Mechanics*, *4*(1), 97–109. https://doi.org/10.1017/S0022112058000331

Casulli, V., & Walters, R. A. (2000). An unstructured grid, three-dimensional model based on the shallow water equations. *International Journal for Numerical Methods in Fluids*, *32*(3), 331–348. https://doi.org/10.1002/(SICI)1097-0363(20000215)32:3<331::AID-FLD941>3.0.CO;2-C

Cheng, R. T., & Casulli, V. (2001). Evaluation of the UnTRIM model for 3-D tidal circulation (pp. 628–642). Presented at the Estuarine and Coastal Modeling: Proceedings of the Seventh International Conference. Retrieved from https://pubs.er.usgs.gov/publication/70023415

Cheng, Ralph T., Casulli, V., & Milford, S. N. (1984). Eulerian-Lagrangian Solution of the Convection-Dispersion Equation in Natural Coordinates. *Water Resources Research*, *20*(7), 944–952. https://doi.org/10.1029/WR020i007p00944

Fringer, O. B., Gerritsen, M., & Street, R. L. (2006). An unstructured-grid, finite-volume, nonhydrostatic, parallel coastal ocean simulator. *Ocean Modelling*, *14*(3), 139–173. https://doi.org/10.1016/j.ocemod.2006.03.006

Fringer, Oliver B., Dawson, C. N., He, R., Ralston, D. K., & Zhang, Y. J. (2019). The future of coastal and estuarine modeling: Findings from a workshop. *Ocean Modelling*, *143*, 101458. https://doi.org/10.1016/j.ocemod.2019.101458

Garratt, J. R. (1977). Review of Drag Coefficients over Oceans and Continents. *Monthly Weather Review*, *105*(7), 915–929. https://doi.org/10.1175/1520-0493(1977)105<0915:RODCOO>2.0.CO;2

Kim, C.-K., & Park, K. (2012). A modeling study of water and salt exchange for a micro-tidal, stratified northern Gulf of Mexico estuary. *Journal of Marine Systems*, *96–97*, 103–115. https://doi.org/10.1016/j.jmarsys.2012.02.008

Lee, J. (2008). *Three-Dimensional Unstructured Finite Difference and Volume Model for Barotropic Coastal and Estuarine Circulation and Application to Hurricane Ivan (2004) and Dennis (2005)*. University of Florida. Retrieved from https://ufdc.ufl.edu/UFE0013880/00001

Lee, J., Lee, J., Yun, S.-L., & Oh, H.-C. (2017). Development of a finite volume two-dimensional model and its application in a bay with two inlets: Mobile Bay, Alabama. *Continental Shelf Research*, *146*, 13–27. https://doi.org/10.1016/j.csr.2017.08.002

Leith, C. E. (1971). Atmospheric Predictability and Two-Dimensional Turbulence. *Journal of the Atmospheric Sciences*, *28*(2), 145–161. https://doi.org/10.1175/1520-0469(1971)028<0145:APATDT>2.0.CO;2

Lentine, M., Grétarsson, J. T., & Fedkiw, R. (2011). An unconditionally stable fully conservative semi-Lagrangian method. *Journal of Computational Physics*, *230*(8), 2857–2879. https://doi.org/10.1016/j.jcp.2010.12.036

Liu, Y. (1988). *Two-dimensional finite-difference model for moving boundary hydrodynamic problems*. University of Florida. Retrieved from http://aquaticcommons.org/1069/

Lynch, D. R., & Gray, W. G. (1978). Analytic Solutions for Computer Flow Model Testing, 1409–1428.

Lynch, D. R., & Officer, C. B. (1985). Analytic test cases for three-dimensional hydrodynamic models. *International Journal for Numerical Methods in Fluids*, *5*(6), 529–543. https://doi.org/10.1002/fld.1650050604

MacWilliams, M. L., & Gross, E. S. (2013). Hydrodynamic Simulation of Circulation and Residence Time in Clifton Court Forebay. *San Francisco Estuary and Watershed Science*, *11*(2). https://doi.org/10.15447/sfews.2013v11iss2art1

MacWilliams, M. L., Bever, A. J., Gross, E. S., Ketefian, G. S., & Kimmerer, W. J. (2015). Three-Dimensional Modeling of Hydrodynamics and Salinity in the San Francisco Estuary: An Evaluation of Model Accuracy, X2, and the Low–Salinity Zone. *San Francisco Estuary and Watershed Science*, *13*(1). https://doi.org/10.15447/sfews.2015v13iss1art2

MacWilliams, M. L., Ateljevich, E. S., Monismith, S. G., & Enright, C. (2016). An Overview of Multi-Dimensional Models of the Sacramento–San Joaquin Delta. *San Francisco Estuary and Watershed Science*, *14*(4). https://doi.org/10.15447/sfews.2016v14iss4art2

Mungkasi, S., & Roberts, S. G. (2012). Approximations of the Carrier–Greenspan periodic solution to the shallow water wave equations for flows on a sloping beach. *International Journal for Numerical Methods in Fluids*, *69*(4), 763–780. https://doi.org/10.1002/fld.2607

Oliveira, A., & Baptista, A. M. (1998). On the role of tracking on Eulerian-Lagrangian solutions of the transport equation. *Advances in Water Resources*, *21*(7), 539–554. https://doi.org/10.1016/S0309-1708(97)00022-5

Smith, S. D. (1980). Wind Stress and Heat Flux over the Ocean in Gale Force Winds. *Journal of Physical Oceanography*, *10*(5), 709–726. https://doi.org/10.1175/1520-0485(1980)010<0709:WSAHFO>2.0.CO;2

Sobey, R. J. (2009). Wetting and drying in coastal flows. *Coastal Engineering*, *56*(5), 565–576. https://doi.org/10.1016/j.coastaleng.2008.12.001

Staniforth, A., & Côté, J. (1990). Semi-Lagrangian Integration Schemes for Atmospheric Models—A Review. *Monthly Weather Review*, *119*(9), 2206–2223. https://doi.org/10.1175/1520-0493(1991)119<2206:SLISFA>2.0.CO;2

Willmott, C. J. (1982). Some Comments on the Evaluation of Model Performance. *Bulletin of the American Meteorological Society*, *63*(11), 1309–1313. https://doi.org/10.1175/1520-0477(1982)063<1309:SCOTEO>2.0.CO;2

Zhang, Y. J., Ateljevich, E., Yu, H.-C., Wu, C. H., & Yu, J. C. S. (2015). A new vertical coordinate system for a 3D unstructured-grid model. *Ocean Modelling*, *85*, 16–31. https://doi.org/10.1016/j.ocemod.2014.10.003

Zhang, Y. J., Ye, F., Stanev, E. V., & Grashorn, S. (2016). Seamless cross-scale modeling with SCHISM. *Ocean Modelling*, *102*, 64–81. https://doi.org/10.1016/j.ocemod.2016.05.002